Molecular Evolution in Collapsing Prestellar Cores III: Contraction of A Bonnor-Ebert Sphere

Yuri Aikawa

Department of Earth and Planetary Sciences, Kobe University, Kobe 657-8501, Japan

Eric Herbst

Departments of Physics, Chemistry, and Astronomy, The Ohio State University, Columbus, OH 43210, USA

Helen Roberts[1]

Department of Physics, The Ohio State University, Columbus, OH 43210, USA

and

Paola Caselli

Osservatorio Astrofisco di Arcetri, Largo Enrico Fermi 5, I-50125 Firenze, Italy

ABSTRACT

The gravitational collapse of a spherical cloud core is investigated by numerical calculations. The initial conditions of the core lie close to the critical Bonnor-Ebert sphere with a central density of $\sim 10^4$ cm^{-3} in one model ($\alpha = 1.1$), while gravity overwhelms pressure in the other ($\alpha = 4.0$), where α is the internal gravity-to-pressure ratio. The $\alpha = 1.1$ model shows reasonable agreement with the observed velocity field in prestellar cores. Molecular distributions in cores are calculated by solving a chemical reaction network that includes both gas-phase and grain-surface reactions. When the central density of the core reaches 10^5 cm^{-3}, carbon-bearing species are significantly depleted in the central region of the $\alpha = 1.1$ model, while the depletion is only marginal in the other model. The two different approaches encompass the observed variations of molecular distributions in different prestellar cores, suggesting that molecular distributions can be probes of contraction or accumulation time scales of cores. The central enhancement of the NH_3/N_2H^+ ratio, which is observed in some prestellar cores, can be

---

[1]Present address: Department of Physics, UMIST, PO Box 88, Manchester M60 1QD, UK

reproduced under certain conditions by adopting recently measured branching fractions for N_2H^+ recombination. Various molecular species, such as CH_3OH and CO_2, are produced by grain-surface reactions. The ice composition depends sensitively on the assumed temperature. Multi-deuterated species are included in our most recent gas-grain chemical network. The deuterated isotopomers of H_3^+ are useful as probes of the central regions of evolved cores, in which gas-phase species with heavy elements are strongly depleted. At 10 K, our model can reproduce the observed abundance ratio of ND_3/NH_3, but underestimates the isotopic ratios of deuterated to normal methanol.

Subject headings: stars: formation — ISM: molecules — ISM: clouds — ISM: individual (L1544, L1517B, L1498, L1521E, L1689B)

1. Introduction

Theoretical models show that molecular abundances in molecular clouds are time-dependent (e.g. Prasad & Huntress 1980). Taking advantage of this dependence, the ages of cloud cores have been estimated. For example, cores with a high abundance of CCS and carbon chain species are considered to be young, while those with large abundances of NH_3 are considered old (Suzuki et al. 1992). There have been arguments, however, on the reliability of such "chemical clocks", because molecular abundances depend not only on the elapsed time but also on density, temperature, and the C/O ratio in the gas phase (e.g. Pratap et al. 1997; Terzieva & Herbst 1998). Moreover, single-dish observations, by which radio astronomers used to estimate molecular abundances, average cloud structure and abundances over a beam size.

During the last decade, independent and spatially-resolved estimates of molecular abundance, temperature, and density have become available. Observations of sub-millimeter continua and extinctions of background stars have revealed density distributions in a variety of starless dense cores (Ward-Thompson et al. 1994; Alves et al. 2001), showing that the density is almost constant inside a radius of several thousand AU, and decreases outside of this radius as r^{-p}, where p is $2.0 - 2.5$ and r is the distance from the core center. Spatial distributions of molecular line intensities have been obtained by interferometric observations and detailed mapping via single dish telescopes. Intensity ratios of different transitions show that the starless cores are almost isothermal with $T \sim 10$ K (Tafalla et al. 1998, 2002, 2004), although a slight deviation of a few K may exist (Evans et al. 2001; Galli et al. 2002). Spatial distributions of molecular abundances within selected cores have been obtained by analyses that include radiative transfer, showing that CO, CS and CCS are depleted at the

core center, while NH_3 and N_2H^+ maintain relatively constant abundances (Caselli et al. 1999; Ohashi et al. 1999; Bergin et al. 2001; Caselli et al. 2002a; Tafalla et al. 2002, 2004). The central depletion indicates that adsorption of gas-phase species onto grain occurs, a process that had long been anticipated theoretically (Watson 1976; Burke & Hollenbach 1983; Tielens & Allamandola 1987). Since adsorption lowers gas-phase molecular abundances as a function of time, it can be used as another indication of the history of the source (Bergin & Langer 1997).

Considering that dense starless cores should be formed from lower density gas at $10^3 - 10^4$ cm^{-3}, we can estimate the contraction time scale via chemical models that include adsorption. Aikawa et al. (2001) and Aikawa et al. (2003) investigated the distribution of molecules in contracting cores by adopting a Larson-Penston (L-P) flow and analogues with slower rates of contraction. They found the central depletion to be greater in models with slower rates of contraction. The L-P model better reproduces observed molecular column densities, while the radial distributions of molecules are better reproduced by a contraction that is three-fold slower. Since predicted molecular column densities vary as contraction proceeds, Aikawa et al. (2003) were able to use their results to sort observed cores into an evolutionary sequence. Mono-deuterated species were also included in their chemical model. They obtained very high D/H ratios such as $H_2D^+/H_3^+ > 1$, which is consistent with the recent observation of H_2D^+ in the core L1544 (Caselli et al. 2003). The L-P flow, however, is an asymptotic solution, which appears in the central region of a collapsing core. The collapse velocity at outer radii, which is of interest in the comparison with observation, is overestimated in the L-P flow. In their models with slower rates of contraction, Aikawa et al. (2003) adopted a constant factor f to decrease the contraction speed. In reality, the factor f varies with time. To avoid this problem, Li et al. (2002) and Shematovich et al. (2003) directly coupled calculations of molecular evolution with magnetized core collapse. They showed that the molecular column densities in L1544 are well reproduced by the magnetized model. Although the infall velocities obtained in their models are generally faster ($\gtrsim 0.2$ km s^{-1}) than observed in L1544 (~ 0.1 km s^{-1}), the magnetized model gives a somewhat smaller, and thus better, infall velocity than the non-magnetized model. They also suggested that the molecular line widths will vary depending on the spatial distribution of the abundances and radial velocity.

The present paper is an update of Aikawa et al. (2003). We now calculate molecular distributions while solving for the contraction of a spherical core numerically, rather than by adopting an L-P flow, so that our infall velocities can be compared with observed values. For simplicity, we restrict ourselves to the non-magnetized case; this simplification enables us to separate the dynamics and chemistry and thus to utilize a large chemical network. The infall speed is dependent on the ratio between the gravitational and pressure forces, for which we

consider two different cases. We will show that observed infall velocities are reproduced, without the help of a magnetic field, if the initial condition of the core is close to the critical Bonnor-Ebert sphere (Bonnor 1956) with central density $\sim 10^4$ cm^{-3}. On the other hand, magnetic fields are probably needed in more massive or less pressurized cores to maintain the infall speed close to observed values. Our newly calculated molecular distributions are presented in selected stages of contraction and compared with recent observations of prestellar cores such as L1498, L1517B, L1521E, and L1544. As shall be shown, our model reproduces some observed features including an enhancement of the NH$_3$/N$_2$H$^+$ ratio in the central regions, which was not explained in previous studies.

Our basic chemical model contains a large gas-phase network (e.g. Terzieva & Herbst 1998) that includes mono-deuterated species, and grain-surface reactions. In addition, we have extended the network for some calculations to include multi-deuterated species (Roberts, Herbst, & Millar 2003). In recent years several multi-deuterated species have been detected in prestellar and protostellar cores, and their relative abundances to normal isotopomers, known as D/H ratios, found to be very high ($10^{-3} - 10^{-1}$) (van der Tak et al. 2002; Lis et al. 2002; Parise et al. 2002; Bacmann et al. 2003; Parise et al. 2004). Since the D/H ratio increases significantly as density increases and as gas-phase CO is depleted, it is of interest to see if the abundances of multi-deuterated species can be reproduced in our contracting core models.

The remainder of the paper is organized as follows. A description of the model is given in §2. Numerical results are presented and compared with observations in §3. In §4, we summarize the chemical and kinematic properties of some prestellar cores, and briefly discuss the formation of cores and the role of turbulence. A summary is contained in §5.

2. Model

2.1. Contraction of Cores

We solve the dynamical collapse of a cloud core following Ogino, Tomisaka, & Nakamura (1999). With the assumption of spherical symmetry, the basic equations are described in spherical coordinates by

$$\frac{\partial \rho}{\partial t} + \frac{1}{r^2}\frac{\partial}{\partial r}(r^2 \rho v) = 0 \tag{1}$$

$$\frac{\partial}{\partial t}(\rho v) + \frac{1}{r^2}\frac{\partial(r^2 \rho v^2)}{\partial r} = -\frac{\partial p}{\partial r} + \rho g \tag{2}$$

and

$$g = -\frac{4\pi G}{r^2} \int_0^r \rho r'^2 dr' \tag{3}$$

where

$$p = \rho c_s^2. \tag{4}$$

In equations (1)-(4), t is the time, r is the distance from the center of the core, ρ is the mass density, v is the radial velocity, g is the acceleration due to gravity, G is the gravitational constant, p is the pressure, and c_s is the speed of sound. The gas is assumed to be isothermal with $T = 10$ K.

The equations are solved numerically by the MUSCL-TVD method (van Leer 1977, 1979; Harten 1984), with the numerical flux calculated by the Roe method.

The radial distribution of density in an equilibrium core (i.e., a Bonnor-Ebert sphere) is given by the equations

$$\frac{\partial(\rho c_s^2)}{\partial r} = \rho g \tag{5}$$

and

$$\frac{\partial(r^2 g)}{\partial r} = -4\pi G \rho r^2. \tag{6}$$

The central density of the equilibrium core is set to be $n_H = 2 \times n(H_2) + n(H) = 2 \times 10^4$ cm^{-3}. Away from the center, the density is almost constant within ~ 10000 AU, and decreases outwards when $r \gtrsim 10000$ AU.

To ensure contraction, the initial density distribution is determined by multiplying the equilibrium density distribution by a constant factor α, equal to the ratio of the gravitational force to the pressure force. The initial radial velocity is set to zero all through the core. We consider two cases: $\alpha = 1.1$ and 4.0. The former model simulates the contraction of a nearly-equilibrium core, while the latter case is similar to the L-P flow, which was adopted in Aikawa et al. (2003). A fixed boundary condition ($v = 0$) is adopted at the outer core radius of 0.2 pc, which is slightly larger than the critical radius of an isothermal equilibrium sphere (see also Ogino, Tomisaka, & Nakamura 1999). The mass of the equilibrium core ($\alpha = 1.0$) is then 4.0 $M_\odot$, which is slightly larger than the critical mass (3.9 $M_\odot$) of a sphere with central density $n_H = 2 \times 10^4$ cm^{-3} and kinetic temperature 10 K. Note that by the word "equilibrium", we refer to a density distribution governed by equations (5) and (6); such a distribution, however, is only stable up to a certain critical mass (Bonnor 1956).

2.2. Chemistry

We follow migrating fluid parcels in the contracting cores and solve a chemical reaction network to obtain the molecular evolution in each parcel. The chemical reaction network includes gas-phase reactions, adsorption onto and desorption from dust, and diffusive grain-surface reactions. The gas-phase network is based on the New Standard Model (NSM) (e.g. Terzieva & Herbst 1998) but includes mono-deuterated species. We adopt newly measured branching fractions for the N_2H^+ recombination in the gas phase. Previously it had been assumed that N_2H^+ dissociatively recombines to produce N_2 + H as the sole products. Recently, however, Geppert et al. (2004) measured the products of the recombination to be NH + N and N_2 + H with branching fractions of 65% and 35%, respectively; these values are adopted in our current network.

All neutral species are assumed to be adsorbed when they hit the grain surface with a sticking probability S of unity. The adsorbed species return to the gas phase via thermal desorption and impulsive heating of the grains by cosmic-rays (Léger, Jura, & Omont 1985; Hasegawa & Herbst 1993a). We have adopted the adsorption energies of Hasegawa & Herbst (1993a) but replaced them with experimental data for pure ices when available (see Model B of Aikawa et al. 2001). One exception is CO, for which we assumed a binding energy of 1780 K, which corresponds to adsorption onto polar ice, instead of the value of pure CO ice (960 K). With the assumption of the lower value, the gas-phase CO abundance was calculated to be rather high compared with observed values (see the discussion in Aikawa et al. 2003).

A set of grain-surface reactions was taken from Ruffle & Herbst (2000). The reaction rate coefficients for the diffusive grain-surface reactions were calculated following Hasegawa & Herbst (1993a) as modified by Stantcheva, Caselli, & Herbst (2001) and Caselli et al. (2002b). The unmodified rate coefficients are proportional to the sum of the rates for the two reactants to diffuse over the entire grain (Hasegawa & Herbst 1993a). Activation energies against diffusion are obtained as a constant fraction (30 %) of adsorption energies, and the diffusion rate is given by the larger of the tunneling and thermal hopping rates. If, for reactions without chemical activation energy, the calculated diffusion rates are larger than both the accretion and evaporation rates, they are replaced by the larger of the latter two. The dominant alteration is to slow down the reaction rates of atomic hydrogen and deuterium. The so-called modified rate method used here has been found to be in good agreement for most species with a more detailed stochastic method (Stantcheva & Herbst 2004). Note that the diffusion barriers and adsorption energies used here are different from those used in the gas-grain models of Ruffle & Herbst (2000, 2001), where higher values were chosen, based on an extrapolation of the analysis of Katz et al. (1999).

The present paper includes two corrections to the grain-surface reaction rates adopted

in our previous paper (Aikawa et al. 2003). Firstly, we now estimate the tunneling rate from activation energies against diffusion $E_{\rm b}$ using a simple rectangular barrier (e.g. Herbst 1993). In Aikawa et al. (2003) the tunneling rates of some species (H, D, H_2, HD, He, C, N, and O) were estimated using the width of the lowest energy band $\triangle E$; the rate is $\pi \triangle E/2h$, where h is the Planck constant (Tielens & Allamandola 1987). The former gives slower tunneling rates than the latter. Secondly, if a reaction between two minor surface species has a chemical activation barrier, we now compare the total reaction rate coefficient, instead of the diffusion rate, with the larger of the accretion and evaporation rates. For reactions between reactive accreting species (e.g. H) and weakly reactive major surface species (e.g. CO) with an activation energy barrier, we utilize a modified version of an additional correction proposed by Caselli et al. (2002b) if the surface abundance of the weakly reactive species accumulates to the point that the probability of reaction exceeds unity in the shorter of the accretion and evaporation intervals. The modification is to replace the standard rate law with one containing the accretion rate of the accreting species (or the evaporation rate if larger) multiplied by the surface abundance of this species and the probability that it reacts with the particular weakly reactive species of interest. Consider, for example, the reaction of H atoms with CO and H_2CO molecules in the limit when both have sufficiently large abundances to turn on the correction, and suppose that the surface abundance of CO is nine times that of formaldehyde. Since the activation energy barriers are the same, the probability that H reacts with CO (0.9) is nine times the probability that it reacts with formaldehyde (0.1). Without the probability term, the reaction rates for H with both CO and H_2CO are the same since the abundance of the weakly reactive species is no longer in the rate law. Because it is very difficult to incorporate the probability term into a full-scale gas-grain model, we have chosen to neglect it. The result is difficult to gauge but, in any case, the use of the modification at this level is certainly preferable to ordinary rate equations (Stantcheva & Herbst 2004). We have used the modification for O + CO and for the reactions of H and D atoms with CO, C_2H_6, CH_4, H_2CO, H_2S, and their deuterated counterparts. All of these reactions except for those involving CO and H_2CO are hydrogen abstraction processes, in which the reacting H atom removes an atom from the other reactant.

Deuterium exchange reactions in the gas phase are based on the work of Millar, Bennett, & Herbst (1989). In including deuterium fractionation on dust particle surfaces, we have assumed that the adsorption energy and barrier against diffusion for surface D atoms are slightly higher than the values for H atoms (Caselli et al. 2002b). In total, our chemical network consists of 878 species and 11779 gas-phase and surface reactions. In §3.4.2, we present results based on a new chemical network extended to include multi-deuterated species (Roberts, Herbst, & Millar 2004). Since we are interested in the D/H ratios of specific

species, such as H_2CO and NH_3, and since a calculation of the fully-multi-deuterated network is time-consuming, complex species such as long carbon chains have been excluded from this network, which consists of 518 species and 12616 reactions.

We have utilized the so-called "low-metal" values for initial gas-phase elemental abundances (see Table 1 of Aikawa et al. 2001) and have adopted the "standard" value of $\zeta = 1.3 \times 10^{-17}$ s^{-1} for the ionization rate by cosmic rays. Considering that the cores we are modeling are embedded in molecular clouds, we assume the visual extinction A_v to be 3 mag at the outer boundary of the core, so that photodissociation does not significantly affect our results. All heavy elements are assumed to be initially in atomic and ionized form, with carbon ionized and oxygen neutral. The initial form of hydrogen is molecular, and the deuterium is assumed to be in the form of HD, at a ratio of 3.0×10^{-5} with respect to H_2.

3. Results

3.1. Core Contraction

Figure 1 (a) shows the temporal variation of the central density. The central densities of the cores with $\alpha = 1.1$ and 4.0 reach 3×10^7 cm^{-3} at ages of 1.17×10^6 yr and 1.82×10^5 yr, respectively. In the former case, the central density reaches 8×10^4 cm^{-3} (initial density of the $\alpha = 4.0$ model) at $\sim 8.45 \times 10^5$ yr and takes another 3.27×10^5 yr to reach a density of 3×10^7 cm^{-3}. The core with the larger α contracts faster, because gravity overwhelms the thermal pressure.

Distributions of number density and infall velocity at the initial central density and when the central density is $3 \times 10^5, 3 \times 10^6$, and 3×10^7 cm^{-3} are shown in Figure 1 $(b - e)$. In these panels, the density and velocity are plotted vs r rather than vs $\log r$. If the density distribution had been plotted as a function of $\log r$, the density would appear to be almost constant at $r \lesssim r_{\text{flat}}$ and to decrease as $n_H \propto r^{-p}$ at larger radii. The exponent p is ~ 2.3 for $\alpha = 1.1$ and ~ 1.9 for $\alpha = 4.0$. The model with the larger α has the larger r_{flat}. When the central density is $n_H = 3 \times 10^5$ cm^{-3}, for example, r_{flat} is about 4.0×10^3 AU and 5.4×10^3 cm^{-3} for $\alpha = 1.1$ and 4.0, respectively.

The infall velocity is naturally zero at the core center, because there is no point source of gravity at $r = 0$. It is also zero at the outermost radius (0.2 pc, or 4.1×10^4 AU) as a fixed boundary value. The infall velocity hence has a peak value at a certain radius, which moves inwards as the contraction proceeds. At the same central density, the model with the larger α has the larger infall velocities. It should be noted that if the contraction starts from a nearly-equilibrium state such as given by $\alpha = 1.1$, the infall velocity when the central

density is $\sim 10^5$ cm^{-3} is in reasonable agreement with the observed values of $0.05 - 0.1$ km s^{-1} of some prestellar cores (Lee, Myers, & Tafalla 2001; Tafalla et al. 2004). Although the peak infall velocity (0.093 km s^{-1}) with $\alpha = 1.1$ and a central density of 3×10^5 cm^{-3} is close to the upper boundary of the observed values (~ 0.1 km s^{-1}), it could be smaller with a smaller α. For example, the peak infall velocity is 0.073 km s^{-1} at the same central density if α is 1.05. In addition, the observation may underestimate the infall velocity by a factor of 1-2, because of morphological effects (Lee, Myers, & Tafalla 2001).

Since the non-zero infall velocities increase as time progresses, the contraction can be said to accelerate with time. In the model with $\alpha = 1.1$, the peak value of the infall velocity becomes comparable to that of the L-P flow (i.e. three times the sound velocity) at a central density of 10^{17} cm^{-3} (Figure 3 of Ogino, Tomisaka, & Nakamura 1999). Because the contraction speeds up, the model is different from the L-P analogues with constant delaying factor f (Aikawa et al. 2003); the current model corresponds to the case in which f decreases with time.

The infall velocities in our model with $\alpha = 1.1$ tend to be smaller than those of Li et al. (2002) and Shematovich et al. (2003), in spite of the fact that our model does not include magnetic support. The difference seems to be caused by a combination of factors including the mass, size, and initial density of the model cores. Since their model cores are initially supported by thermal *and* magnetic pressure, and extend to 10^5 AU, they are more massive (20 $M_\odot$) than our model with $\alpha = 1.1$ (4.4 $M_\odot$). The importance of mass is discussed by Shematovich et al. (2003), who show that infall velocities in their 10 $M_\odot$ model are smaller than those of their 20 $M_\odot$ model. The initial central density of Li et al. (2002) is 10^3 cm^{-3}, while it is $\sim 10^4$ cm^{-3} in our models. If we lower our initial central density to 10^3 cm^{-3}, the peak value of the infall velocity is 0.16 km s^{-1} when the central density reaches 2×10^5 cm^{-3}. This velocity is only slightly smaller than the value (0.2 km s^{-1}) of Li et al. (2002). The boundary condition at the outermost radius also affects the infall velocity. While we have adopted a fixed boundary condition, Li et al. (2002) adopted a free-pressure boundary condition, which yields larger infall velocities.

It is interesting that the infall velocities of our core model are similar to, although slightly larger than, those derived in the MHD model of Ciolek, & Basu (2000), which show good agreement with the observed line width in L1544 (Caselli et al. 2002c). Specifically, when their central density reaches values of 4×10^5 cm^{-3}, 4×10^6 cm^{-3}, and 4×10^7 cm^{-3}, the peak infall velocity of their neutral component is 0.1 km s^{-1} (at $\sim 1.3 \times 10^4$ AU), 0.14 km s^{-1} (at $\sim 5.0 \times 10^3$ AU), and 0.17 km s^{-1} (at $\sim 2.0 \times 10^3$ AU), respectively.

3.2.   Molecular Distributions

Figure 2 and Figure 3 show calculated distributions of molecular (fractional) abundances in contracting cores when the central density is 3×10^5 cm^{-3} (top), 3×10^6 cm^{-3} (middle), and 3×10^7 cm^{-3} (bottom) for the models with $\alpha = 1.1$ and 4.0, respectively. Gas-phase species are on the left panels and ice mantle species on the right. Only the region inside 2×10^4 AU is shown, because densities at larger radii are not high enough to be distinguished from the ambient gas in observations.

The molecular abundance distributions in L1498, L1517B, L1521E, L1689B, and L1544 have been estimated by Tafalla et al. (2002), Lee et al. (2003), Tafalla et al. (2004), and Tafalla & Santiago (2004) based on the intensity map of dust continuum and molecular lines. The distributions in L1498, L1517B and L1544 are shown in Figure 4 for a comparison with our model results. Note that the five objects have different central densities: $n(\mathrm{H}_2) =$ 9.4×10^4 cm^{-3} in L1498, 2.2×10^5 cm^{-3} in L1517B, 2.7×10^5 cm^{-3} in L1521E, 1×10^6 cm^{-3} in L1689B, and 1.4×10^6 cm^{-3} in L1544, although these values should be taken with caution because they depend on the somewhat uncertain core temperature. Indeed, if the center of L1544 is as cold as 7 K, for example, the central density increases to $\sim 10^7$ cm^{-3} (Evans et al. 2001; Zucconi et al. 2001).

It is clear that CO and CS are significantly depleted at the centers of the three cores shown in Figure 4. But the extent of depletion is not so clear because the observations are not sensitive to very low abundances at the center. For example, we cannot tell the real CO distribution within $\lesssim$ 7000 AU from the observations of CO line intensities. Tafalla et al. (2004) observed L1517B and L1498 with higher angular resolution than Tafalla et al. (2002), and found that their data are consistent with a step function distribution, as can be seen in Figure 4. The degree of depletion of CO and CS in the central regions should therefore be taken with caution. Contrary to the three sources shown in Figure 4, no CO depletion is found in L1521E (Tafalla & Santiago 2004) and little depletion is found in L1689B (Lee et al. 2003). So, a successful dynamic/chemical model must be able to explain this duality of results concerning depletion.

Below we discuss our calculated distributions of individual species in some detail, grouped by class of molecules. We first compare radial distributions of molecular abundances obtained in our models with the observations. Comparison via integrated molecular column densities is discussed in a later subsection.

3.2.1. C-bearing species

As expected from previous theoretical work (e.g. Aikawa et al. 2003), the central depletion of gaseous CO and other C-bearing species is more significant at later stages of contraction and in the model of slower contraction ($\alpha = 1.1$). At higher densities, the time scale for adsorption onto grains is shortened, while a slower contraction gives more time for adsorption and gas-phase destructive reactions (especially for so-called 'early-time' species) to be effective. The distributions of gas-phase species in the model with $\alpha = 4.0$ are similar to those in the L-P model of Aikawa et al. (2003), which is reasonable considering the similarity of the dynamics (§2).

The distributions of CO and CS in our $\alpha = 1.1$ model are in reasonable agreement with those in L1517B and L1544 at the appropriate central core densities. Although a more detailed comparison via intensity profiles would be desirable considering the uncertainties in the observational estimates of their central abundances, the model with $\alpha = 1.1$ is clearly in better agreement with these cores than the $\alpha = 4.0$ model. On the other hand the shallower distributions in L1521E are similar to the $\alpha = 4.0$ case (Tafalla & Santiago 2004). Note that L1521E and L1517B have similar central densities.

Several interpretations are possible for this difference in the molecular abundances. If contraction is ignored, as in pseudo-time-dependent models, the degree of CO depletion at the core center is a function of time. The adsorption time scale is given by $[\pi a^2 \sqrt{\frac{8kT}{\pi m}} n(\text{grain})]^{-1} \sim 2 \times 10^4 (\frac{n_\text{H}}{3 \times 10^5 \text{cm}^{-3}})$ yr, where a is the grain radius (0.1 μm), k is the Boltzmann constant, T is the temperature (10 K) and m is the mass of the CO molecule. Hence the central region of L1517B should be older and that of L1521E should be younger than a few 10^4 yr, which is the most naive interpretation. However the density structures of the cores are not constant in reality; since the central densities of these prestellar cores are high ($\gtrsim 10^5$ cm^{-3}), they have been formed from the ambient low-density ($10^3 - 10^4$ cm^{-3}) component by contraction. Given the similar central densities, the distribution of molecular abundances should also be similar, if the contraction rate is similar in both sources. It is then likely that any difference in the central depletion should probe the difference in contraction, and hence the ratio of the gravitational force to the pressure force. There is a caveat to this line of reasoning, however: if the central region of L1517B is colder than that of L1521E, then the former may indeed be denser and its central depletions higher. On the other hand, unless the central density of L1521E is much less than 10^5 cm^{-3}, the absence of significant CO depletion puts a rather strong constraint on its dynamical age.

3.2.2. N-bearing species

Because of the low adsorption energy of their precursor molecule N_2 on grain surfaces, the depletion of NH_3 and N_2H^+ is less significant than that for other heavy-element species (Bergin & Langer 1997; Aikawa et al. 2001, 2003). Let us first discuss a more detailed feature: the ratio of NH_3 to N_2H^+. For L1517B and L1498, Tafalla et al. (2002, 2004) found the N_2H^+ abundance to be almost constant but NH_3 to increase towards the center by a factor of ~ 15. A smaller enhancement of ~ 3 is also observed in L1544 (Tafalla et al. 2002). Since both species are formed mainly from N_2 and since the molecular ion, N_2H^+, is not considered to be adsorbed onto grains directly, the central enhancement of NH_3/N_2H^+ seems puzzling, and previous models have not shown such an enhancement. In our $\alpha = 1.1$ model, on the other hand, the NH_3/N_2H^+ ratio indeed increases inwards when the central density is $n_H = 3 \times 10^5$ cm^{-3}, which is similar to the value in L1517B and L1498. An analogous enhancement towards the inner radius can also be seen in the region of 2500 AU $\lesssim r \lesssim 10000$ AU in our models with $\alpha = 1.1$ and 4.0 when the central density is 3×10^6 cm^{-3}, a density similar to the value in L1544. The enhancement in our models is caused by the newly adopted branching ratio for the N_2H^+ recombination, which is discussed in §2.2. At large radii, where gas-phase CO is abundant, N_2H^+ is destroyed mainly by proton transfer to CO. The product, N_2, reacts with H_3^+ to reform N_2H^+, but in the central regions, where CO is depleted, N_2H^+ mainly recombines to produce NH, which is then transformed to NH_3 by reactions with H_3^+ and H_2. The chemical pathways are detailed in Figure 5. The rate coefficient of N_2H^+ + CO is 1.5×10^{-9} cm^3 s^{-1}, while that of N_2H^+ + e $\rightarrow$ NH + N is 2.4×10^{-6} cm^3 s^{-1}. Hence NH_3 enhancement occurs when the abundance ratio n(CO)/n(e) becomes smaller than $\sim 10^3$.

Now let us consider the individual radial distributions of protonated nitrogen and ammonia for α=1.1. As can be seen in Figure 2, at a central density of 3×10^5 cm^{-3}, both N_2H^+ and NH_3 are *not* seriously depleted towards the center. When the central density is raised to 3×10^6 cm^{-3}, however, the species are depleted at $r \lesssim 2500$ AU. This result contradicts the observation of Tafalla et al. (2002), who found their abundances to be almost constant (with a slightly enhanced NH_3/N_2H^+ ratio inwards) in L1544, which possesses a central core density in excess of 10^6 cm^{-3}. It should be noted, however, that a detailed analysis by other researchers suggests that N_2H^+ and NH_3 could be depleted at the center of this source (Caselli et al. 2003). Belloche & André (2004) also found that N_2H^+ is depleted in the center of the cold protostellar core IRAM 04191, where the density n_H is $\gtrsim 10^6$ cm^{-3}.

In our model, the depletion of NH_3 and N_2H^+ is caused by a combination of adsorption of N_2 and N onto grains and transformation of N atoms to NH_3 on grain surfaces, where it remains given its high binding energy of 3080 K. Even with our chosen low adsorption energy

for N_2 of 750 K, the rate of adsorption for this species is larger than the cosmic-ray induced desorption rate when the density n_H is $\gtrsim 10^6$ cm^{-3}. However, the rate of cosmic-ray induced desorption is quite sensitive to the choice of adsorption energy. If we adopt an even smaller adsorption energy for N_2, and if hydrogenation of N atom is less efficient (see §3.2.3 for a discussion on grain-surface reactions), the depletion of NH_3 and N_2H^+ will not occur until later stages of contraction, when the higher density leads to a higher rate of adsorption.

Although we reproduce the central enhancement of the NH_3/N_2H^+ ratio, the relevant central NH_3 abundances calculated in our $\alpha = 1.1$ model are higher than the observed values shown in Figure 4 by around an order of magnitude. On the other hand, the calculated abundance of N_2H^+ is in reasonable agreement with the results for all three cores shown in Figure 4. To change the abundance of ammonia while maintaining the same abundance of N_2H^+, one should not change the abundance of the molecular nitrogen mother molecule or the cosmic ray ionization rate since these parameters will affect both species. Ammonia in the gas phase is formed from N^+, which is in turn formed by the cosmic-ray ionization of N atoms in early stages of contraction and by $N_2 + He^+$ in later stages (Figure 5). If the rate coefficients for processes leading to N^+ formation are smaller than assumed in our model, the NH_3 abundance become smaller, without affecting N_2H^+.

3.2.3. Ice Composition

The abundances of major species in ice mantles are shown in the right panels of Figure 2 and Figure 3. With some important exceptions, it can be seen that the abundances do not vary much with radius, especially compared with the radial dependence of heavy gas-phase species. In addition, the dependence on time, or central density, is not significant when the central density is higher than 3×10^5 cm^{-3}. Mantle species are formed both by direct adsorption from the gas and by grain-surface reactions. As an example of surface formation, adsorbed CO is hydrogenated to form HCO, which is further transformed to H_2CO, and CH_3OH on grain surfaces by reactions with atomic hydrogen. The peak abundance of CH_3OH in the gas-phase is 7×10^{-12}, which is much lower than its ice abundances. Carbon dioxide in ice mantles is formed mainly by a surface reaction between O and HCO on grain surfaces. In our model, the activation barrier of this reaction is assumed to be zero. Hence it is more efficient than another CO_2-forming reaction, CO + O, for which we have assumed an activation barrier of 1000 K. This older value is somewhat higher than the value of 290 K measured by Roser et al. (2001) on amorphous ice. Use of this lower value at 10 K does not result in significant changes to our results.

The ice composition in dense prestellar cores has not been observed so far, because of

the faintness of background stars. Instead, we compare our model results with observations towards low-mass protostars and field stars. Although the central densities of our model cores are very high ($\gtrsim 10^5$ cm^{-3}), the density at $r \sim 20000$ AU is as low as $n_{\rm H} \sim 6 \times 10^3$ cm^{-3}, which is comparable to that of the foreground material in front of these stars. So we can compare our surface predictions for this large radius. It is customary to describe abundances of various surface species relative to H_2O ice. With this convention, Table 1 summarizes ice compositions observed towards the field star Elias 16, the low-mass protostar Elias 29, and the high-mass protostars NGC 7538 IRS9, GL 7009S and W33A (Ehrenfreund & Shutte 2000; Gibb et al. 2000). It can be seen that carbon monoxide and carbon dioxide ices are relatively abundant toward these sources. The abundance of CH_3OH is high towards high-mass protostars, while it is low towards the field star Elias 16 and the low-mass protostar Elias 29. It should be noted, however, that solid CH_3OH has recently been detected with an abundance of $15 - 25$ % towards three low-mass YSO's (Pontoppidan et al. 2003).

Listed in the right three columns of Table 1 are ice compositions at $r = 20000$ AU in the model with $\alpha = 1.1$ and central density of 3×10^6 cm^{-3}. With our 10 K model, the density at this radius remains slightly under 10^4 cm^{-3}. We varied the temperature of the core, since portions of the gas in front of the sources considered here may well be warmer than 10 K. Although the contraction time scale depends on the sound velocity within the core, the dynamics have been assumed to be the same as the 10 K model with $\alpha = 1.1$ in order to probe only the chemical effects. Distributions of molecular abundances for models with $T = 12$ K and 15 K are shown in Figure 6 . The predicted ice composition depends sensitively on the temperature, because of the low adsorption and migration energies of reactant species such as H atoms.

We first compare the $T = 10$ K model with observations towards Elias 16, which correspond to the ice composition in a cold quiescent cloud. The calculated abundances of CO and NH_3 are consistent, but the CH_3OH abundance is higher and the CO_2 abundance significantly lower than the observed values. The model with $T = 15$ K, on the other hand, gives a high CO_2 abundance and little CO. Since there are temperature variations within a molecular cloud, a mixture of $T = 10 - 15$ K components may reproduce the observed CO and CO_2 abundances better. However, such a mixture would give too much CH_3OH. The material in front of Elias 16 may well have lower gas densities than considered here; lower-density results toward the edge of our model core indeed show lower methanol abundances. Next we compare our models with low- and high-mass protostars. Both a warm envelope and cold foreground component exist along the observed line of sight so that, on average, the temperature of the matter along the line of sight towards these sources may be higher than that towards Elias 16. The calculated abundances of NH_3 and CH_3OH ices in our models with $T = 12$ and 15 K are consistent with the observations, and a mixture of these two

models can reproduce the CO_2 abundance. However, the CO and H_2CO abundances are significantly underestimated.

Although the possible temperature variation along the observed line of sight makes the comparison difficult, it seems that our model generally underestimates CO at $T > 10$ K, and CO_2 and H_2CO at $T < 15$ K. In the models with $T = 12$ and 15 K, CO ice is transformed to CH_3OH and CO_2 by grain-surface reactions in manner that seems to be too efficient. Destruction of CO would be suppressed if we take into account the recent experimental results that CO hydrogenation occurs only within several surface layers, because H atoms cannot penetrate deep into ice mantles (Hidaka et al. 2004; Watanabe et al. 2004, Chigai et al. in prep). Such an effect can be accounted for with the so-called three-phase approach of Hasegawa & Herbst (1993b). In order to improve the model, it would also be useful to calibrate the rate-equation formula for the grain surface reactions. Although the ice composition calculated by the modified-rate method is in good agreement with that by stochastic methods (Caselli et al. 2002b; Stantcheva & Herbst 2004), a small grain-surface-reaction network (i.e. including less than a few tens of reactions) is used in such comparisons. On the other hand, our current model includes more than 500 grain-surface reactions (with deuterium species). Calibration of the modified-rate method with a stochastic method using a large reaction network is desirable.

3.3. Molecular Column Densities

In order to derive molecular radial distributions from the observational data, one has to solve a (non-LTE) radiation transfer problem with some assumptions such as the density and velocity distributions. For easier and more straightforward comparison between observational data and theoretical models, it is useful to calculate molecular column densities integrated along the line of sight in the models. Table 2 lists column densities of assorted gas-phase molecular species in our models with $\alpha = 1.1$ and 4.0 when the central density is 3×10^5, 3×10^6, and 3×10^7 cm^{-3}. We first integrate the absolute molecular abundance (i.e. number density) along the line of sight to obtain a column density at each impact parameter, and then average them within the beam size of the IRAM 30 m telescope, except for NH_3, H_3^+ and H_2D^+. The column density of NH_3 is averaged over a radius of 20", and H_3^+ and H_2D^+ are averaged over a radius of 11", considering the beam sizes of the Effelsberg and CSO telescopes, respectively.

As can be seen in Table 2, the column densities of carbon-bearing species do not vary with time while the central density increases from 3×10^5 cm^{-3} to 3×10^7 cm^{-3}. Although the central depletion becomes heavier as contraction proceeds, contributions from the outer

Table 1.   Ice Composition in Molecular Clouds and Protostellar Cores [a]

Species	field star Elias 16	low-mass PS[b] Elias 29	NGC 7538 IRS9	high-mass PS GL 7009S	W33A	10 K	model 12 K	15 K
H_2O	100	100	100	100	100	100	100	100
CO	34	5.6	16	15	8	29	0.01	0.4
CO_2	15	22	20	21	13	0.6	0.5	68
CH_4	-	< 1.6	2	4	1.5	3.3	5.6	5.8
CH_3OH	< 3.4	< 4	5	30	18	5.8	37	9.5
H_2CO	-	-	2	3	6	10^{-4}	0.01	0.4
NH_3	< 6	< 9.2	13	-	15	0.4	17	18

[a]Ehrenfreund & Shutte (2000); Gibb et al. (2000)

[b]PS stands for protostar.

Table 2.   Molecular Column Densities (cm^{-2}) of Gaseous Species in Theoretical Models

Species	$n_H = 3 \times 10^5$ cm^{-3}	alpha=1.1 3×10^6 cm^{-3}	3×10^7 cm^{-3}	3×10^5 cm^{-3}	alpha=4.0 3×10^6 cm^{-3}	3×10^7 cm^{-3}
CO	1.9(17)[a]	1.9(17)	2.0(17)	1.2(18)	1.0(18)	1.0(18)
C_3H_2	9.8(12)	8.7(12)	8.8(12)	2.2(14)	1.6(14)	1.5(14)
H_2CO	5.1(13)	4.6(13)	4.6(13)	1.1(15)	7.9(14)	7.3(14)
CH_3OH	5.9(10)	5.3(10)	5.3(10)	9.6(12)	4.3(12)	3.5(12)
CCS	7.5(11)	6.9(11)	6.9(11)	2.5(13)	1.8(13)	1.7(13)
CS	1.1(13)	1.0(13)	1.0(13)	6.6(13)	5.4(13)	5.2(13)
SO	3.2(11)	3.5(11)	3.9(11)	1.6(13)	1.5(13)	1.4(13)
HCN	1.0(15)	8.0(14)	7.8(14)	5.5(14)	7.9(14)	7.3(14)
HC_3N	7.4(12)	5.8(12)	5.8(12)	5.1(13)	4.4(13)	4.1(13)
NH_3	6.2(15)	7.8(15)	7.4(15)	7.0(14)	4.8(15)	5.4(15)
N_2H^+	1.1(13)	1.8(13)	2.0(13)	5.5(12)	2.6(13)	3.5(13)
N_2D^+	1.7(12)	4.2(12)	5.2(12)	5.5(11)	6.7(12)	1.1(13)
HCO^+	2.9(13)	2.9(13)	3.0(13)	1.4(14)	1.3(14)	1.3(14)
DCO^+	2.3(12)	2.4(12)	2.6(12)	1.0(13)	1.4(13)	1.3(13)
H_3^+	5.3(13)	6.3(13)	5.9(13)	3.9(13)	5.3(13)	5.4(13)
H_2D^+	2.3(13)	6.3(13)	7.9(13)	9.1(12)	4.3(13)	7.4(13)

[a]$a(b)$ means $a \times 10^b$.

radii keep the molecular column densities almost constant. In order to estimate the evolutionary stage (i.e. central density) of a core from these species, a comparison with the radial abundance distribution is more useful. On the other hand, many of the column densities have a clear dependence on α; they are higher in the model of larger α, where the contraction is faster.

As opposed to the behavior of carbon-bearing species, the column densities of nitrogen-bearing and deuterated species increase as the central density rises. This dependence is more significant in the model with larger α. The depletion of N_2H^+ and NH_3 becomes significant only inside $r \sim 2500$ AU and in a late stage of contraction, because of the low adsorption energy of their mother molecule N_2. As the central density increases from 3×10^5 to 3×10^7 cm^{-3}, the radial distributions of the N_2H^+ and NH_3 abundances relative to hydrogen do not change much in the region of 2500 AU $\lesssim r \lesssim$ 5000 AU (Fig. 2 and Fig. 3), which means that their absolute abundances there increase as the core contracts.

Table 3 shows estimated central densities and determined molecular column densities in some prestellar cores. The column density of N_2H^+ is in agreement with our models ($\alpha = 1.1$ and 4.0) within a factor of a few, except for L1521E, which has a very low N_2H^+ column density in spite of its relatively high central density. If the central density is of order 10^5 cm^{-3}, the larger α is preferred for L1521E. The ammonia abundance, and thus its column density, are mostly overestimated in our models, as discussed in the previous subsection. The column density of CCS is better reproduced in the model with $\alpha = 4.0$. The $\alpha = 1.1$ model better reproduces the CS column density in L1498 and L1517B, while $\alpha = 4.0$ is preferred for CS in L1544. However, comparison of these S-bearing species should be taken with caution, because their abundances depend on the assumed elemental abundance of sulfur and chemical network (e.g. NSM or UMIST) (Aikawa et al. 2003). The observed CO column densities are in reasonable agreement with our model results when $\alpha = 1.1$.

3.4. Deuterium Fractionation

3.4.1. Mono-deuterated Species

Mono-deuterated species and deuterium fractionation are included both in gas-phase and grain-surface reactions in our chemical reaction network (Aikawa et al. 2003, and references therein). In low-temperature cores, molecular D/H ratios are enhanced by exothermic exchange reactions such as $H_3^+ + HD \rightarrow H_2D^+ + H_2$, in which the backwards endothermic reactions are too slow to be of importance. Since the main reactant of H_2D^+ is CO, the D/H ratios are further enhanced by CO depletion. Although the back reaction between H_2D^+

+ H_2 can be speeded up by the presence of ortho-H_2 (Gerlich et. al. 2002; Walmsley et al. 2004), this process is not included in our model. If ortho-H_2 is abundant, molecular D/H ratios would become smaller than predicted here. Computed spatial distributions of mono-deuterated species and their normal counterparts are shown in Figure 7 and Figure 8 for models with $\alpha = 1.1$ and 4.0, respectively. Molecular D/H ratios are higher in the model with smaller α, which shows a heavier CO depletion. The difference is especially significant at an earlier stage of contraction, with a lower central density.

Let us now consider some important D/H ratios. For $\alpha = 1.1$, the atomic D/H ratio in the central region is as high as 0.23 and 0.37 when the central density is 3×10^6 cm^{-3} and 3×10^7 cm^{-3}, respectively. The high abundance of D atoms enhances the deuteration of ice-mantle species in spite of the slower migration of D atoms compared with that of H atoms on grain surfaces. The D/H ratio for the molecular ion H_2D^+ in the gas phase is higher than unity at the core center when the central density is $\gtrsim 10^6$ cm^{-3} for both values of α. The H_2D^+ fractional abundance of $\sim 10^{-9}$ at the appropriate central core density obtained in our model with $\alpha = 1.1$ is consistent with the observation in L1544 (Caselli et al. 2003). While Caselli et al. (2003) and van der Tak (2004) estimate that the H_2D^+ fractional abundance at the 20" off-set position is smaller than the central value by a factor of $2-5$, its abundance at $r \sim 3000$ AU (which corresponds to 20" assuming a distance of 150 pc) is calculated to be smaller than the central value by a factor of 1.5 when the central density is 3×10^6 cm^{-3}. Note that the calculated fractional abundance of H_2D^+ is relatively high even in the latest contraction stage, when the central density is 3×10^7 cm^{-3} in our model, but will promptly decrease when the gas is heated by a newly born protostar, because the endothermic backwards reaction between H_2D^+ and H_2 will begin to turn on. Hence we conclude that H_2D^+ is a good probe of starless cores immediately prior to star formation.

How do our results compare with observation of other singly deuterated species? Caselli et al. (2002a) obtained column density ratios for $N(DCO^+)/N(HCO^+)$ and $N(N_2D^+)/N(N_2H^+)$ towards the dust peak of L1544 of 0.04 and 0.2, respectively. In our model with $\alpha = 1.1$ and a central density of 3×10^6 cm^{-3}, the calculated column density ratios are $N(DCO^+)/N(HCO^+) = 0.08$ and $N(N_2D^+)/N(N_2H^+) = 0.2$ (Table 2), both in reasonable agreement with the observed values. These results for singly-deuterated species can be changed when multiple deuteration is considered; the calculated D/H ratios for DCO^+ and N_2D^+, however, are larger by only a factor of 1.5 in the multi-deuterated model discussed below.

3.4.2. Multi-deuterated Species

In recent years, multi-deuterated species have been detected in several prestellar and protostellar cores. For example, van der Tak et al. (2002) and Lis et al. (2002) detected ND_3 and derived relative abundances of $n(ND_3)/n(H_2) \sim 10^{-12} - 10^{-11}$ and $n(ND_3)/n(NH_3) \sim 10^{-3}$ in NGC 1333 and Barnard 1. Bacmann et al. (2003) obtained $n(D_2CO)/n(H_2) \sim 10^{-11}$ and $n(D_2CO)/n(H_2CO) \sim 0.01 - 0.1$ in several prestellar cores. In addition, the mono-, doubly-, and triply-deuterated methanol isotopomers CH_2DOH, CHD_2OH and CD_3OH have abundances of 0.3 ± 0.05, 0.06 ± 0.01, and 0.014 ± 0.006 relative to their normal counterpart, respectively, in the protostar IRAS 16293 (Parise et al. 2004, B. Parise personal communication). These highly-deuterated methanol isotopomers are considered to be formed by grain-surface reactions in the prestellar stage and desorbed when the core is heated by a newly born star. As shown in the previous subsection, our model produces high abundances of mono-deuterated species, including atomic deuterium, which is important for subsequent deuteration on grain surfaces. Hence it is interesting to see if we can also obtain large enhancements for multi-deuterated species.

The left and middle panels in Figure 9 show radial distributions of assorted gas-phase species and their singly and multiply deuterated isotopomers obtained from our $\alpha = 1.1$ model. Comparison of the calculated D/H ratio with the observed value is tricky; while the molecular D/H ratios increase, the abundances of most gas-phase species relative to hydrogen decrease inwards. One should calculate molecular column densities considering the core structure, in order to compare the model results with observations.

Let us focus attention on D_2CO and ND_3. Since the critical densities of the observed D_2CO transitions ($J = 2 - 1$ and $J = 3 - 2$) are relatively high ($\gtrsim 10^5$ cm^{-3}), the observed abundances are compared with our results in the central regions. In particular, we calculated the column densities of H_2CO and D_2CO in the region of $n_H \geq 2 \times 10^5$ cm^{-3} by integrating along the line of sight, and then obtained the column density ratio, which is $\sim 7 \times 10^{-3}$ throughout our range of central densities 3×10^5 cm$^{-3} - 3 \times 10^7$ cm^{-3}, when the CO depletion factor ($N(H_2)/N(CO) \times 10^{-4}$) is $12 - 250$. On the other hand, Bacmann et al. (2003) obtained D_2CO/H_2CO column density ratio of 0.01-0.14 (including error bars) in prestellar cores with the CO depletion factor of ~ 15. Although the peak abundance of D_2CO in our $\alpha = 1.1$ model is similar to the observed value ($\sim 10^{-11}$) in these prestellar cores, the D_2CO/H_2CO ratio is clearly underestimated. Evaporation of D_2CO and H_2CO from ice mantles does not improve the agreement in the gas phase, since the surface abundance ratio for D_2CO/H_2CO is lower than that in the gas phase. This disagreement is not found in the stationary shell deuterium-fractionation model of Roberts, Herbst, & Millar (2004), where the calculated ratio of 0.03 for D_2CO/H_2CO is in good agreement with that measured for L1544. The higher

fractionation stems partially from the use of the UMIST RATE99 network of reactions (Le Teuff et al. 2000; Roberts, Herbst, & Millar 2004).

NGC 1333 and Barnard 1, in which ND_3 is observed, harbor protostars. Since the protostellar stage is not included in our model, we compare our results at the latest stage, at which a central density of 3×10^7 cm^{-3} is reached, with observations. The abundance ratio of ND_3 and NH_3 varies significantly with radius. The beam size of the ND_3 observations is 25", which corresponds to a spatial resolution of ~ 8800 AU assuming that the distance to the objects is 350 pc. Hence we calculate the column density ratio of ND_3 and NH_3 averaged over a radius of 4400 AU; the ratio is 2×10^{-3} and is in reasonable agreement with observations. It should be noted that our peak abundance of ND_3 is $\sim 10^{-10}$, which is much higher than the observed values ($\sim 10^{-11}$). As we discussed in §3.2.2, our model overestimates the abundance of NH_3. If we could reduce the abundance of N^+, both NH_3 and ND_3 abundances would be decreased without affecting their abundance ratio.

The distributions of ice-mantle isotopomers are shown in the right panels of Figure 9. In the central region of the core with a central density of $\gtrsim 3 \times 10^6$ cm^{-3}, the abundance ratio of ND_3 to NH_3 is about 10^{-3}. Hence, even if there is some desorption of NH_3 ice in the central region of these protostars, the gas-phase abundance ratio of ND_3/NH_3 remains as high as 10^{-3}.

Now let us consider the deuterium fractionation of methanol in ice mantles. Methanol is formed mainly via grain-surface reactions, in particular the surface hydrogenation of CO by H atoms. In fact its gas-phase fractional abundance in our model is computed to be at most 10^{-11}, which is less than the observed value of 4.4×10^{-9} in IRAS 16293 (van Dishoeck et al. 1995). Hence methanol and its isotopes observed in this object are desorbed from the grain surfaces as a result of heating by a protostar, although the desorption might be significant only in the central regions, because the observed CH_3OH abundance in the gas-phase is much lower than the value expected from the ice composition of CH_3OH/H_2O =15-25% recently obtained towards a low-mass protostar (Pontoppidan et al. 2003). In the right panels of Figure 9, it can be seen that the relative abundances of the multi-deuterated methanol isotopomers to their normal counterpart are lower than the observed values in IRAS 16293. For example, the abundances of surface CHD_2OH (the abundance of which is the same as that of CH_2DOD depicted in Figure 9) and CD_3OH relative to normal methanol (see Figure 9) are calculated to be $\sim 10^{-2}$ and $\sim 10^{-4}$ at the center of our densest core. These values are smaller than the observed values of 0.06 ± 0.01 and 0.014 ± 0.006, respectively, in IRAS 16293 (Parise et al. 2004, B. Parise personal communication). In addition, the singly deuterated methanol CH_2DOH is calculated to be ~ 0.17 times the abundance of normal methanol, which is slightly lower than the claimed ratio of 0.3 ± 0.2 in IRAS 16293. Parise et

al. (2004) concluded that the high abundances of multi-deuterated species are reproduced if the atomic D/H ratio in the gas phase is 0.1-0.3. Although the atomic D/H ratio obtained in our model (left panels of Figure 9) is similar to this value, such a high ratio is obtained only after the adsorption of CO onto grains. Before the atomic D/H ratio becomes high enough, a significant amount of CH_3OH is formed, which lowers the total D/H ratio in methanol.

In order to improve the agreement with the methanol isotopomeric observations, a layered structure of the ice mantle could be important. Because the D/H ratio increases with time and because the desorption rate of CH_3OH is small, those isotopomers formed with low D/H ratio in the early stages will be buried deep in the ice mantle while those with high D/H ratio will be in the surface layers when the protostar is born. Then the latter component will be desorbed first. In fact, the rotational temperature of CH_3OH and its isotopes in IRAS 16293 is ~ 50 K, which suggests that the observed region is not hot enough to desorb the entire ice mantles. This scenario is bolstered by the low observed abundance of CH_3OH in the gas-phase of 4.4×10^{-9} in IRAS 16293 (van Dishoeck et al. 1995) compared with the calculated abundance of CH_3OH ice obtained in our model and the observed ice abundance in some low-mass protostellar cores ($\S3.2.3$). A test for this scenario is the observation of D/H ratios in young hotter cores in which the ice mantles have been completely desorbed but gas-phase chemistry has not yet affected the desorbed species significantly.

It is also interesting to look at our predictions for the abundances of the ions D_2H^+ and D_3^+ at the centers of cores (Figure 9). In agreement with the work of Roberts, Herbst, & Millar (2003), we find that the latter ion is the dominant species of the $H_nD_{3-n}^+$ family at densities $\gtrsim 10^7$ cm^{-3}. The abundance of D_2H^+ is $\sim 10^{-10}$, which is in agreement with the first detection of this species in the prestellar core IRAS 16293E by Vastel et al. (2004). On the other hand, the radial distribution of H_2D^+ is now predicted to be rather flat or even decreasing towards the center (see Figure 9) at a central density of 3×10^6 cm^{-3}, in disagreement with the L1544 observations of Caselli et al. (2003) and van der Tak (2004). This problem also occurs with the static shell model of Roberts, Herbst, & Millar (2004).

4. Discussion

4.1. Chemical and Kinetic Properties of Observed Prestellar Cores

We now revisit the observed properties of the prestellar cores L1498, L1517B, L1521E, and L1544, and discuss which model (i.e. $\alpha = 1.1$ or 4.0) is preferable for each object. The upper part of Table 4 summarizes chemical properties that are described in $\S3.2$. The values in brackets are the preferred α for each property and object. Starting with depletion, we

see that $\alpha = 1.1$ is preferable for reproducing the heavy depletion of CO and CS in L1498, L1517B, and L1544, while the model with $\alpha = 4.0$ accounts for no depletion in L1521E. The abundance ratio of NH_3/N_2H^+ is enhanced towards the core center by a factor of ~ 15 in L1498 and L1517B and by a factor of ~ 3 in 1544. Considering their central densities, $\alpha = 1.1$ is preferable for L1498 and L1517B, while both models ($\alpha = 1.1$ and 4.0) can reproduce the modest enhancement in L1544.

Comparison via molecular column densities are not listed, since these distinctions are less obvious than the spatial distribution; the preferable α varies with species for each object. The molecular column density is directly affected by uncertainties in both observation (e.g. assumed geometry, velocity field and temperature in the analysis) and reaction rate coefficients (§3.3).

The kinematic properties of the objects are listed in the lower part of Table 4. Subtracting the thermal component from the intrinsic line width, the non-thermal components of the N_2H^+ line width are calculated to be 0.17 km s^{-1} in L1498 and L1517B (Tafalla et al. 2002), and 0.27 km s^{-1} in L1521E. Hirota et al. (2002) also obtained a relatively large intrinsic line width of $0.3 - 0.5$ km s^{-1} for species such as C_3S ($J = 4 - 3$) and $H^{13}CO^+$ ($J = 1 - 0$) in L1521E. Infall velocities in L1498 and L1544 are estimated from CS and N_2H^+ lines by Lee, Myers, & Tafalla (2001). Ohashi et al. (1999) observed CCS in L1544, and derived a larger infall velocity (0.1 km s^{-1}) than Lee, Myers, & Tafalla (2001). While $\alpha = 1.1$ is preferable for reproducing the narrow line width and small infall velocities in L1498, L1517B, and L1544, the large widths may be an indication of faster contraction (i.e. $\alpha = 4.0$) in L1521E.

Combining the chemical and kinematic properties, the model with $\alpha = 1.1$ is consistent with L1498, L1517B, and L1544, while the model with $\alpha = 4.0$ is preferable for L1521E. Although it is not listed in Table 4, L1689B could be another example which is fit better by $\alpha = 4.0$. Lee et al. (2003) found that the molecular depletion in L1689B is much less significant than that of L1544, in spite of the fact that their central densities are similar. Molecular line widths in L1689B are also broader, indicating more active kinematics than those in L1544 (Lee et al. 2003).

4.2. Formation of Cores and Role of Turbulence

The line widths of molecular cloud tracers are typically significantly larger than the thermal line width, which suggests that the clouds are dominated by non-thermal motions often identified as turbulence (e.g. Myers & Goodman 1988; Fuller & Myers 1992; Goodman

Table 3. Observed Molecular Column Densities in Assorted Prestellar Cores

Object	central density $n(H_2)$ cm^{-3}	N$_2$H$^+$ 10^{12} cm^{-2}	NH$_3$ 10^{14} cm^{-2}	CCS 10^{12} cm^{-2}	CS 10^{14} cm^{-2}	CO 10^{17} cm^{-2}
L1498	9×10^4	8± 4[a] , 3.0[b]	(4.1)[c,d], 2.3[b]	(16.5)[c]	(0.40)[e] , 0.14[b]	2.4[b]
L1517B	2.2×10^5	3±0.3[a] , 3.1[b]	7[c] , 2.1[b]	8.6[c]	0.13[b]	1.5[b]
L1521E	2.7×10^5	< 1.4[f]	0.73[f]	28[f]	3.0[f]	8.5[f]
L1544	1.4×10^6	9±2[a] , 7.3[b]	1.8[b]	20[g]	0.46[b]	4.0[b] , 12[h]

[a]Caselli et al. (2002d)

[b]Tafalla et al. (2002)

[c]Suzuki et al. (1992)

[d]The column densities with parentheses are observed somewhat ($\sim 30''$) offset from the N$_2$H$^+$ peak.

[e]Hirota et al. (1998), assuming ^{34}S/S= 4.2%

[f]Hirota et al. (2002) and references therein

[g]Ohashi et al. (1999)

[h]Caselli et al. (2002a)

Table 4. Properties of the Observed Prestellar Cores

Parameter	L1498	L1517B	L1521E	L1544
Chemical Properties				
CO depletion	heavy	heavy	no	heavy
	[1.1][a]	[1.1]	[4.0]	[1.1]
CS depletion	heavy	heavy	no	heavy
	[1.1]	[1.1]	[4.0]	[1.1]
NH$_3$/N$_2$H$^+$ central enhancement	yes	yes	...	yes
	[1.1]	[1.1]	...	[either]
Kinematics				
Non-thermal Line width [km s^{-1}]	0.17[b]	0.17[b]	0.27[c]	0.2[b]
Infall Velocity [km s^{-1}]	0.03-0.044[d]			0.021-0.1[d,e]
	[1.1]	[1.1]	[4.0]	[1.1]

[a]A preferred value of α

[b]Tafalla et al. (2002)

[c]Tafalla & Santiago (2004)

[d]Lee, Myers, & Tafalla (2001)

[e]Ohashi et al. (1999)

et al. 1998; Burkert & Bodenheimer 2000). The existence and dissipation of turbulence are considered to be one of the keys controlling star formation (e.g. Ballesteros-Paredes et al. 2003; Mac Low & Klessen 2004). In our present paper, we do not consider turbulence. Since observed molecular line widths in many prestellar cores are dominated by thermal motions (Tafalla et al. 2002; Tatematsu et al. 2004), this simplification is justified at least for those objects.

However, the different values of α in our models can tell us something about the time scale for the ambient material to be accumulated onto the core and for turbulence to dissipate. Although the origin of turbulence is not well understood, turbulence will decay within a sound-crossing time scale, without excitation sources (e.g. Stone, Ostriker, & Gammie 1998). If the accumulation of interstellar gas is efficient and a core becomes too massive to be supported by thermal pressure before turbulence dissipates, it collapses dynamically after the dissipation (i.e. resulting in large α). On the other hand, if the accumulation is rather slow and turbulence dissipates before the core mass reaches the critical value, the core becomes a stable Bonnor-Ebert sphere. Additional accumulation will achieve a critical Bonnor-Ebert core with $\alpha \sim 1$.

As discussed in the previous subsection (see also §3.1 and §3.2), both the line width and molecular distributions obtained in our model with $\alpha = 1.1$ are consistent with the observations in L1517B and L1498. On the other hand, molecular distributions in L1521E are better reproduced by the $\alpha = 4.0$ model. Since observed line widths are relatively large, as predicted in the model, L1521E could indeed be a core with large α. However, a clear infall signature is not observed in this object. Based on the above core formation processes, one possibility is that L1521E has accumulated enough mass to be recognized as a prestellar core before the dissipation of the turbulence. In this case, the turbulence accounts for the relatively large line width, and the relatively fast accumulation (before the turbulence decays) accounts for the *young* ($\lesssim 10^5$ yr) molecular abundances with little or no depletion. Detailed observation of velocity fields in chemically young cores such as L1521E and studies on the origin of turbulence in molecular clouds are highly desirable in order to understand the formation of cores.

5. Summary

We have utilized numerical calculations to investigate the gravitational contraction of spherical cloud cores and the molecular distribution synthesized within these collapsing cores.

Our major findings are that:

- The observed infall velocities in prestellar cores, typically $\sim 0.05 - 0.1$ km s^{-1} when the central density is 10^5 cm^{-3}, are reproduced by the contraction of a core that is initially close to the critical Bonnor-Ebert sphere ($\alpha = 1.1$) with a central density of 2×10^4 cm^{-3}. Note that α is the ratio of the gravitational force to the pressure force, and $\alpha = 1.0$ corresponds to the equilibrium sphere.

- When the central density of the core model with $\alpha = 1.1$ reaches $n_{\mathrm{H}} = 3 \times 10^5$ cm^{-3}, carbon-bearing species are significantly depleted in the central region, which is consistent with observations of L1517B and L1498.

- In the model with $\alpha = 4.0$, the contraction is faster, and hence the depletion of molecules is less significant than in the model with $\alpha = 1.1$. When the central density is 3×10^5 cm^{-3}, the molecular distribution is consistent with that in L1521E. The molecular distribution can thus be a probe of the contraction or accumulation time scale of cores.

- The central enhancement of the NH$_3$ to N$_2$H$^+$ ratio, which is observed in prestellar cores, is reproduced at a central core density of 3×10^5 cm^{-3} by adopting a recently measured branching ratio for the N$_2$H$^+$ dissociative recombination.

- The column densities of carbon-bearing species are higher in the model with larger α, and they tend to vary little with time when the central density of the core is $3 \times 10^5 - 3 \times 10^7$ cm^{-3}. On the other hand, the column densities of N-bearing species and deuterated species tend to increase with contraction.

- Significant deuterium fractionation is obtained, especially when $\alpha = 1.1$. Particularly striking are the D/H ratios of deuterated isotopomers of H$_3^+$, which lie similar to or higher than unity at the core center when the central density is $\gtrsim 3 \times 10^6$ cm^{-3}. The deuterated isotopomers of H$_3^+$ can be useful in probing the central regions of evolved cores in which species containing heavy elements are depleted from the gas.

- In the realm of neutral multi-deuterated species, our model is capable of reproducing the observed abundance ratio of ND$_3$/NH$_3$ found in protostellar objects, but underestimates the deuterium fractionation of formaldehyde and methanol observed in prestellar cores and the protostellar object IRAS 16293.

- The composition of ice mantles depends sensitively on the temperature. While CO ice is dominant in the model with $T = 10$ K, CH$_3$OH and CO$_2$ are the most abundant C-bearing species in ice mantles for the models with $T = 12$ K and 15 K, respectively. In reality, temperature varies with space and time within prestellar cores. Consideration of such temperature variation is important for predicting the ice composition. Evaluation

of relevant grain-surface processes in laboratory experiments and comparison between the modified-rate and stochastic methods using a large grain-surface-reaction network are highly desirable.
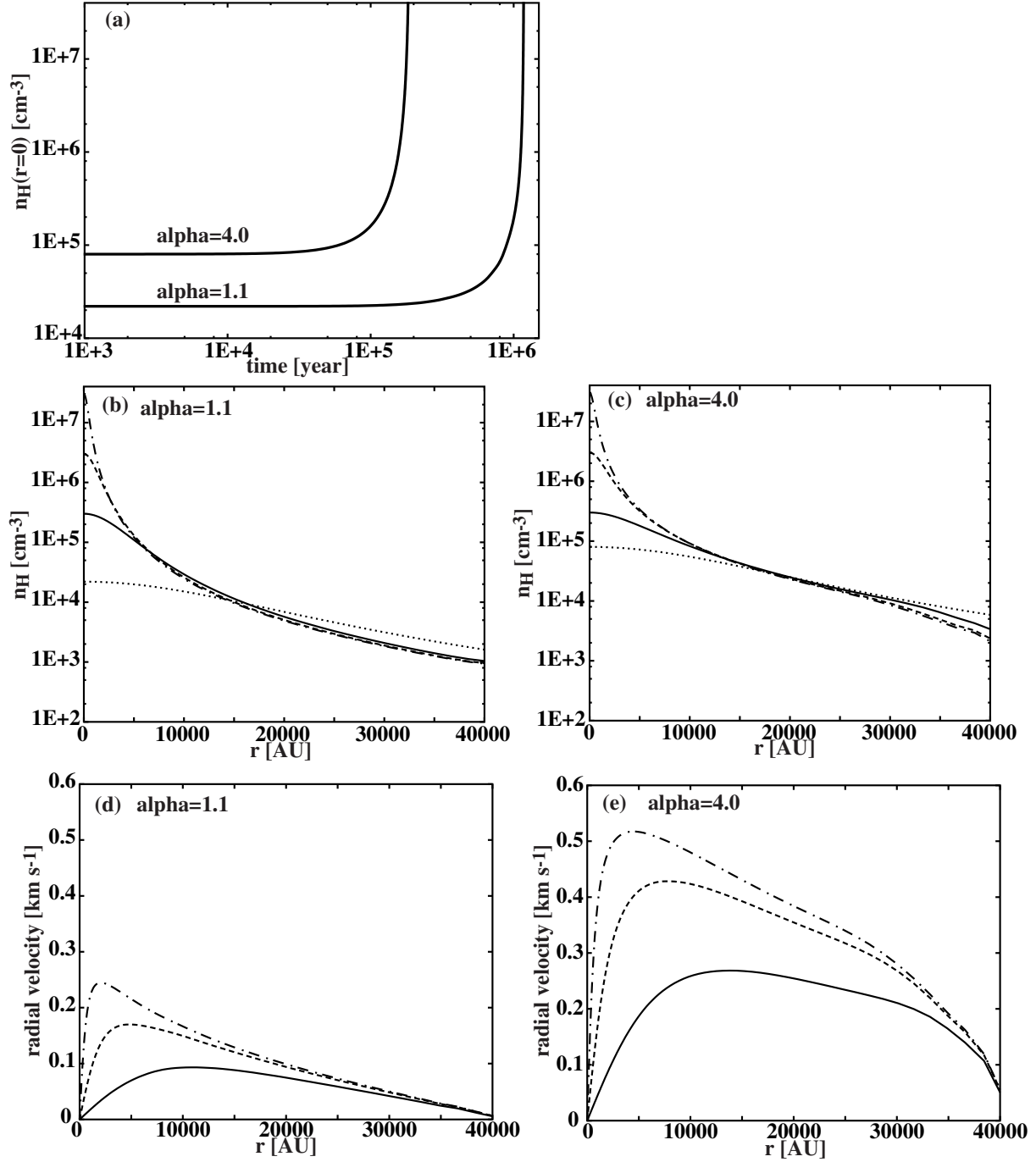
Fig. 1.— The temporal variation of the central number density of the model cores is shown in (a). The initial densities of the model cores are larger than the equilibrium values by a factor of α. The density and velocity distributions in the model with $\alpha = 1.1$ are shown in panels (b) and (d), respectively. The dotted line represents the initial density distribution, while the solid, dashed and dot-dashed lines represent the density and velocity distributions at $t = 1.05 \times 10^6$, 1.15×10^6, and 1.17×10^6 yr. The density and velocity distributions in the model with $\alpha = 4.0$ are shown in panels (c) and (e), respectively. The dotted line represents the initial density distribution, while the solid, dashed and dot-dashed lines represent the density and velocity distributions at $t = 1.29 \times 10^5$, 1.70×10^5, and 1.82×10^5 yr.
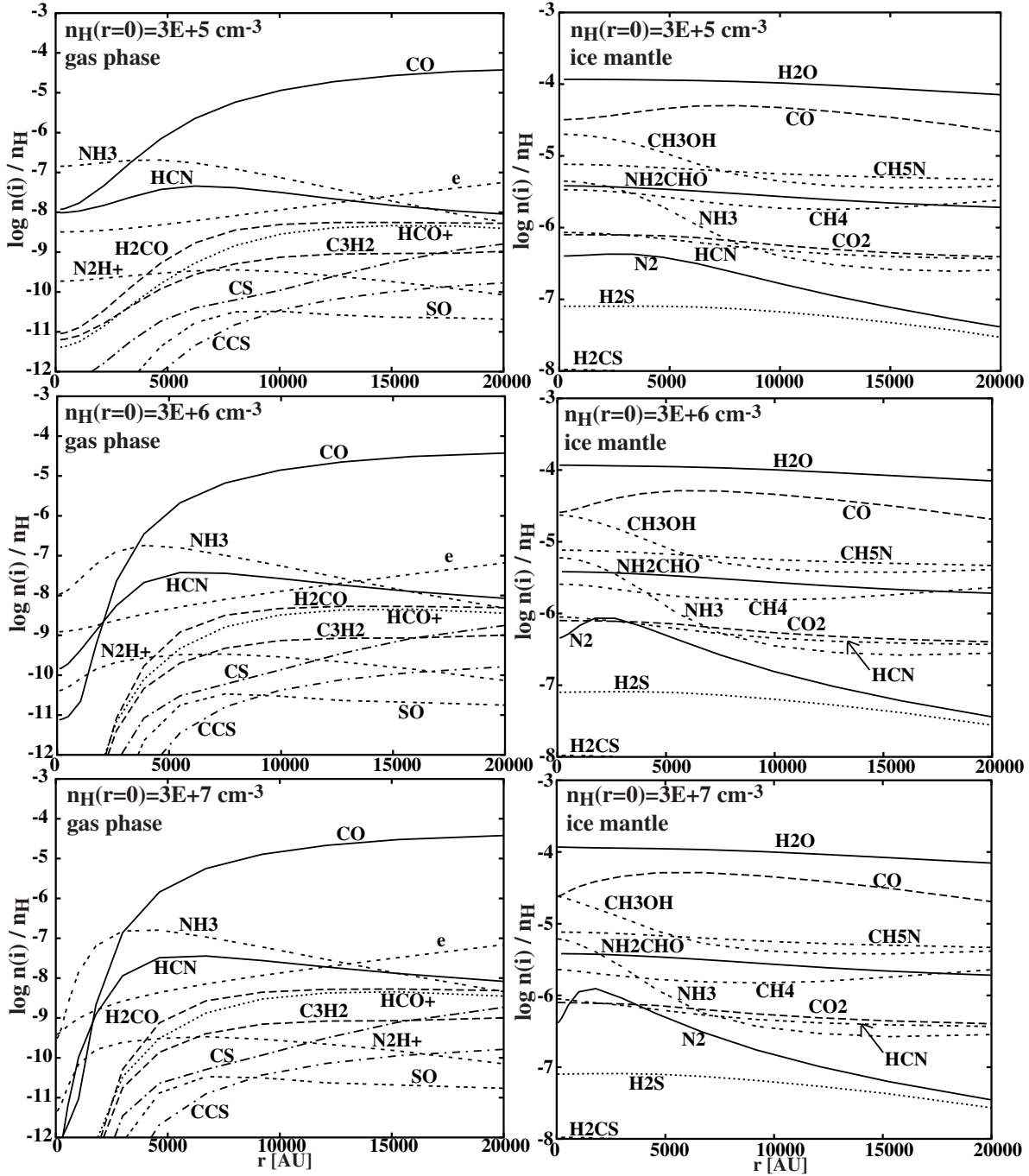
Fig. 2.— Distributions of calculated molecular abundances with $\alpha = 1.1$. The left panels show the gas-phase species, and the right panels show the ice-mantle species. The central densities are 3×10^5 cm^{-3} (top), 3×10^6 cm^{-3} (middle), and 3×10^7 cm^{-3} (bottom).
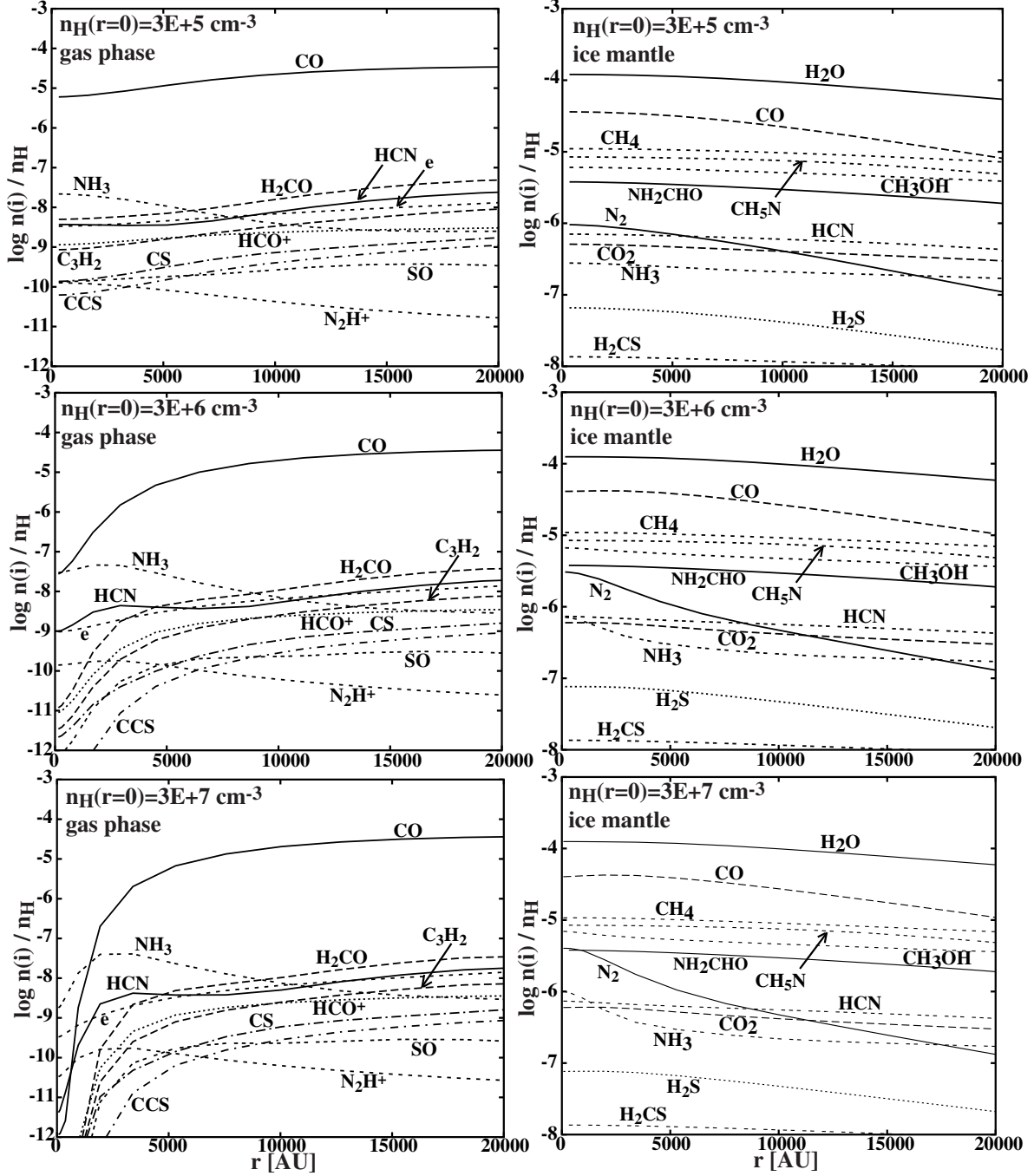
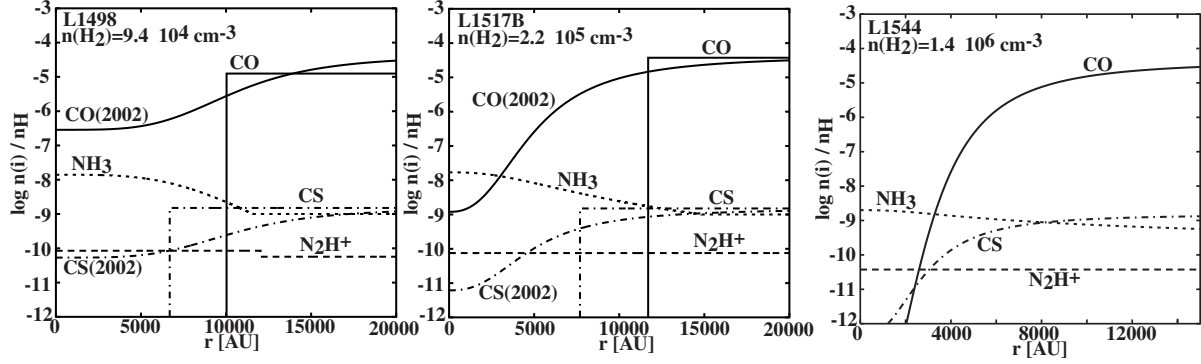Fig. 3.— Distributions of molecular abundances as in Figure 2 but for $\alpha = 4.0$.

Fig. 4.— Estimated molecular distributions in L1498, L1517B, and L1544 by Tafalla et al. (2002; 2004). Abundances of CO and CS estimated by Tafalla et al. (2002) are labeled by CO(2002) and CS(2002). The estimated central density $n(\mathrm{H_2})$ of the core is given in each plot.
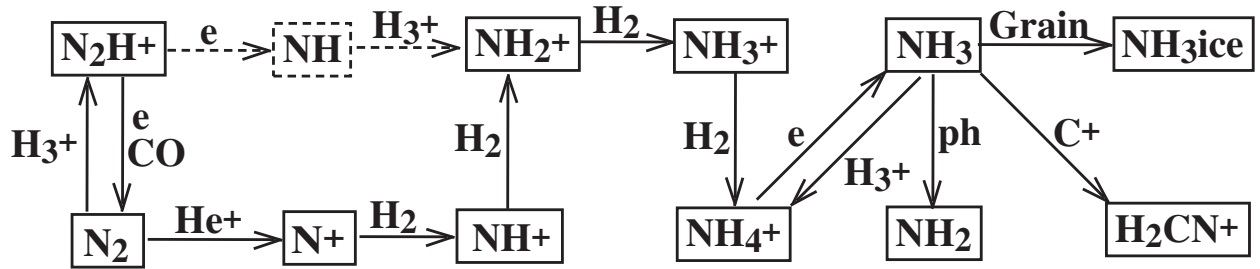
Fig. 5.— Main formation and destruction reactions of $\mathrm{N_2H^+}$ and $\mathrm{NH_3}$ in the gas phase. If CO is depleted, the reactions shown with dashed lines become dominant.
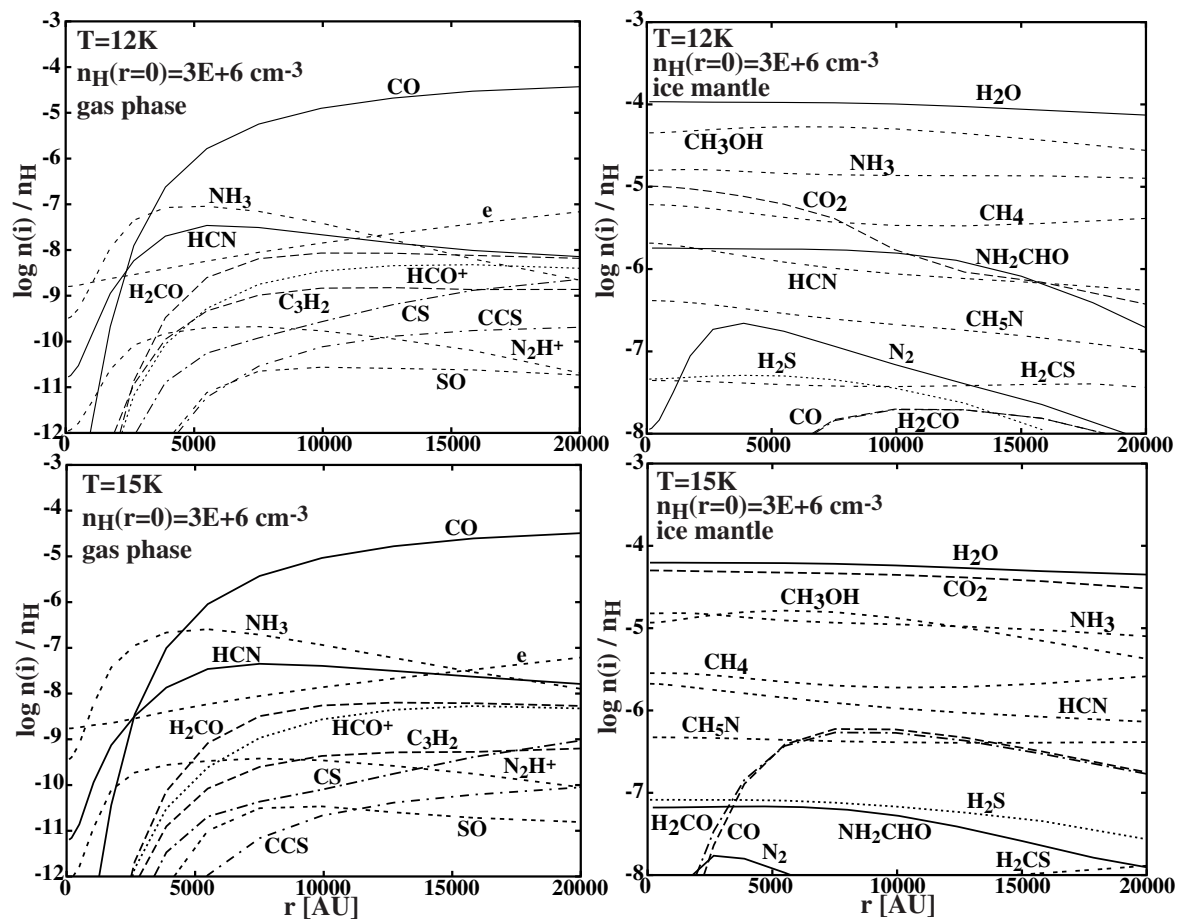
Fig. 6.— Distributions of molecular abundances as in Figure 2 but for $T = 12$ K and 15 K. The central density of the core is 3×10^6 cm^{-3}.
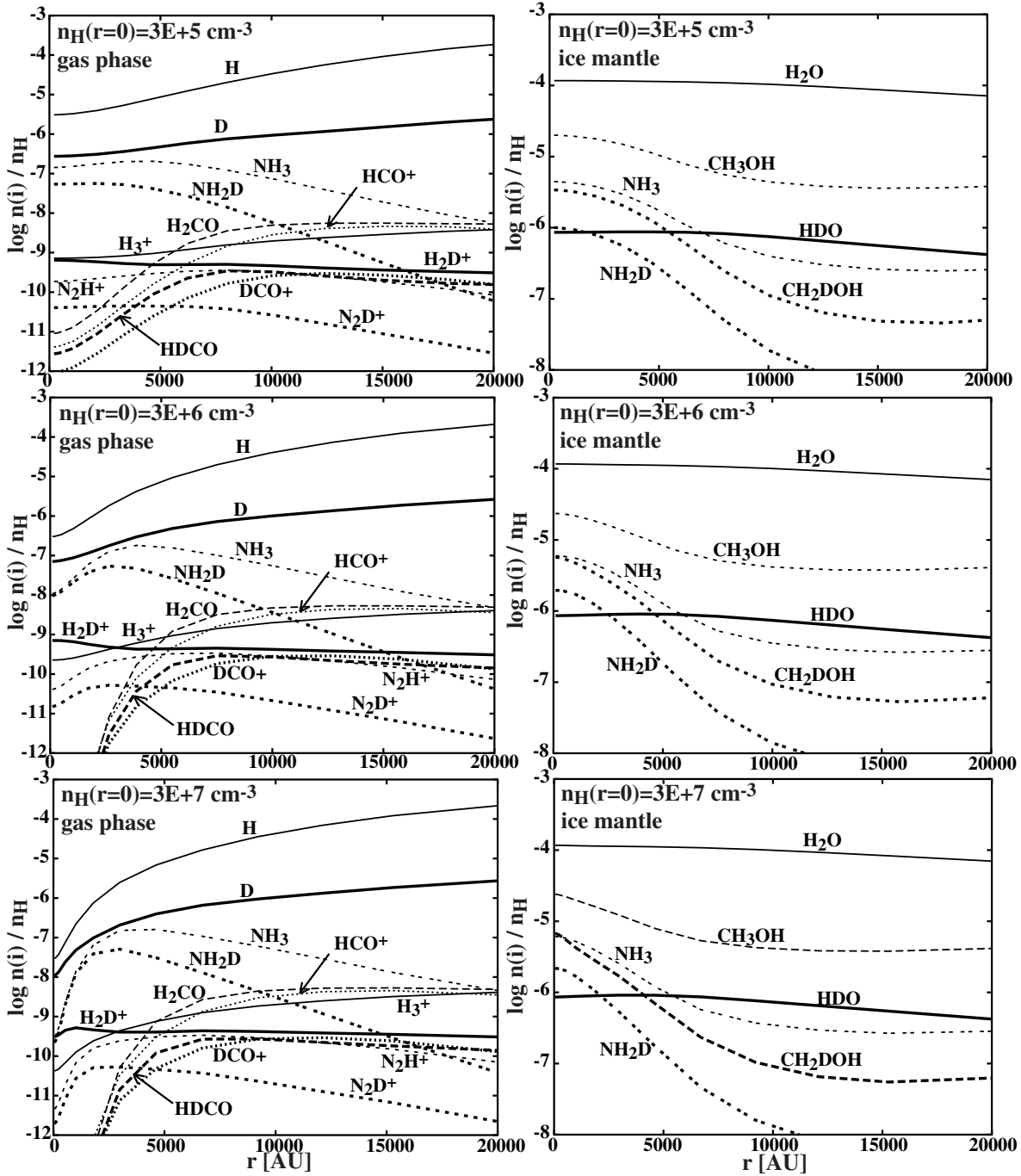
Fig. 7.— Distribution of mono-deuterated species and their normal counterparts with $\alpha = 1.1$. Deuterated species are shown with thick lines while their normal counterparts are shown with thin lines. Isotopomers of the same chemical species are presented by the same type of lines (solid, dashed or dotted). Other details are the same as in Figure 2.
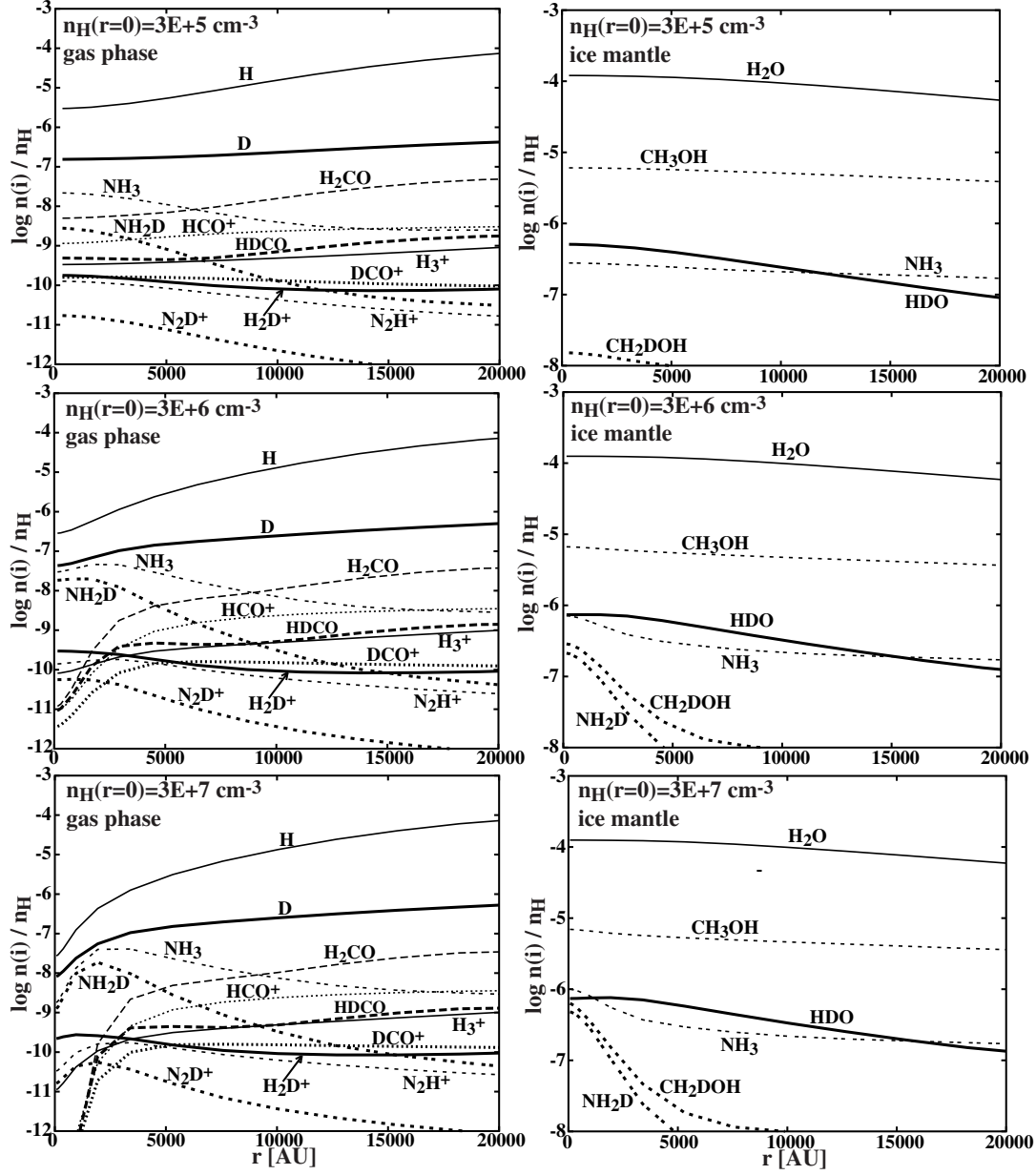
Fig. 8.— Distribution of mono-deuterated species and their normal counterparts as in Figure 7 but for $\alpha = 4.0$.
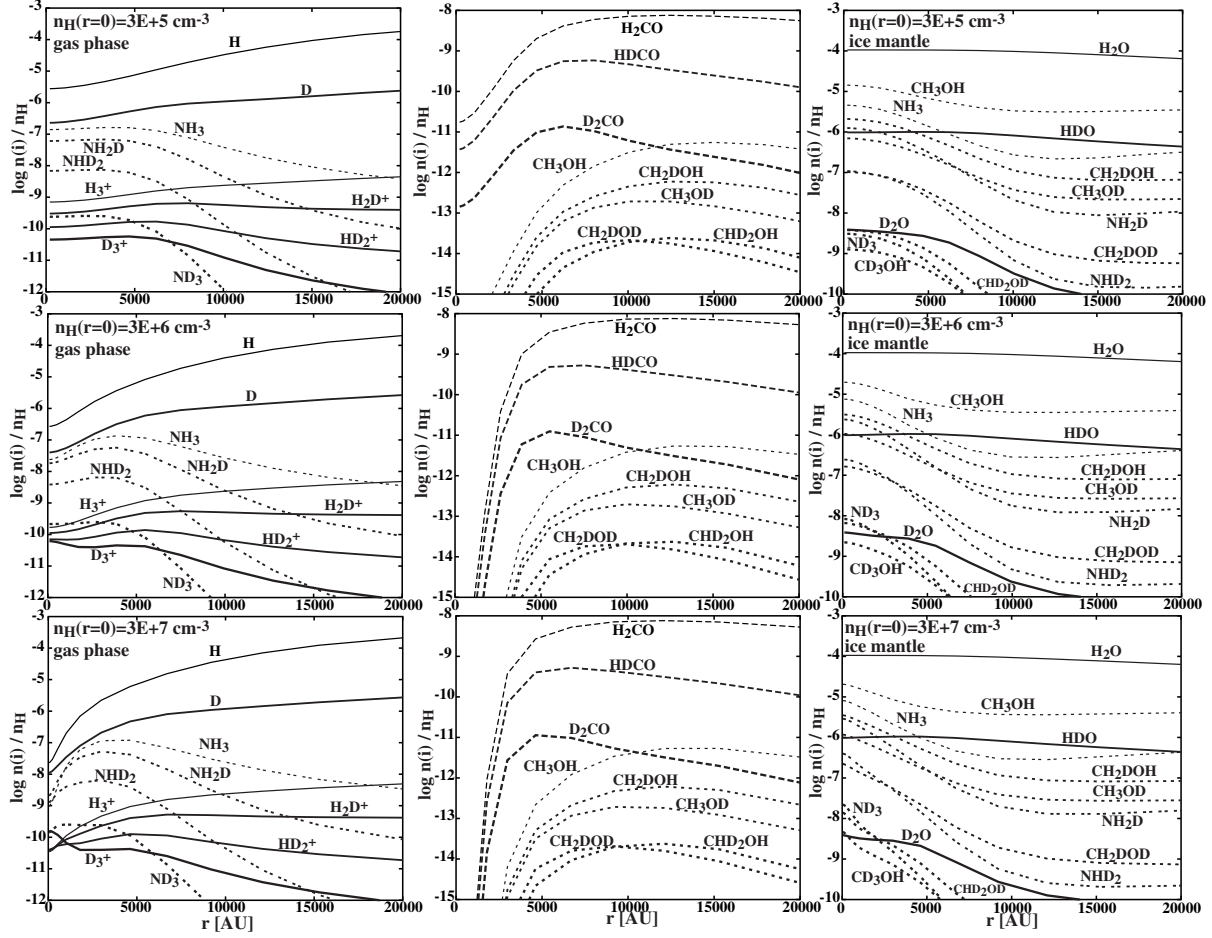
Fig. 9.— Distribution of multi-deuterated species and their normal counterparts with $\alpha = 1.1$. Other details are the same as in Figure 7.

REFERENCES

Aikawa, Y., Ohashi, N., Inutsuka, S.-I., Herbst, E., & Takakuwa, S. 2001, ApJ, 552, 639

Aikawa, Y., Ohashi, N., & Herbst, E. 2003, ApJ, 593, 906

Alves, J. F., Lada, C. J., & Lada, E. A. 2001, Nature, 409, 159

Bacmann, A., Lefloch, B., Ceccarelli, C., Steinacker, J., Castets, A., & Loinard, L. 2003, ApJ, 585, L55

Ballesteros-Paredes, J., Klessn, R. S., & Vázquez-Semadeni, E. 2003, ApJ, 592, 188

Belloche, A., & André, P. 2004, A&A, 419, L35

Bergin, E. A., Ciardi, D. R., Lada, C¿ J., Alves, J., & Lada, E. A. 2001, ApJ, 557, 209

Bergin, E. A. & Langer, W. D. 1997, ApJ, 486, 316

Bonnor, W. B. 1956, MNRAS, 116, 351

Burke, J., & Hollenbach, D. J. 1983, ApJ, 265, 223

Burkert, A., & Bodenheimer, P. 2000, ApJ, 543, 822

Caselli, P., Walmsley, M., Tafalla, M., Dore, L., & Myers, P. 1999, ApJ, 523, L165

Caselli, P., Stantcheva, T., Shalabiea, O., Shematovich, V. I., & Herbst, E. 2002b, Plan. Sp. Sci. 50, 1257

Caselli, P., van der Tak, F. F. S., Ceccarelli, C., & Bacmann, A. 2003, A&A, 403, 37

Caselli, P., Walmsley, C. M., Zucconi, A., Tafalla, M., Dore, L., & Myers, P. C. 2002a, ApJ,565, 344

Caselli, P., Walmsley, C. M., Zucconi, A., Tafalla, M., Dore, L., & Myers, P. C. 2002c, ApJ,565, 331

Caselli, P., Benson, P. J., Myers, P. C., & Tafalla, M. 2002c, ApJ, 572, 238

Ciolek, G. E., & Basu, S. 2000, ApJ, 529, 925

Ehrenfreund, P., & Shutte, W. A. 2000, in Astrochemistry: From Molecular Clouds to Planetary Systems, eds. Minh, Y.C. & van Dishoeck, E.F. (Astronomical Society of the Pacific), p. 135

Evans, N.J.II, Rawlimgs, J.M.C., Shirley, Y. L., & Mundy, L. 2001, ApJ 557, 193

Fuller, G. A., & Myers, P. C. 1992, ApJ, 384, 523

Galli, D., Walmsley, M., & Gonçalves, J. 2002, A&A 394, 275

Geppert, W. D., Thomas, R., Semaniak, J., Ehlerding, F., Millar, T. J., Oesterdahl. F., af Ugglas, M., Djuric, N., Paál, A., & Larsson, M. 2004, ApJ, 609, 459

Gerlich, D., Herbst, E., & Roueff, E. 2002, P&SS, 50, 1275

Gibb, E. L., Whittet, D. C. B., Schutte, W. A., Boogert, A. C. A., Chiar, J. E., Ehrenfreund, P., Gerakines, P. A., Keane, J. V., Tielens, A. G. G. M., van Dishoeck, E. F., & Kerkhof, O. 2000, ApJ, 536, 347

Goodman, A. A., Barranco, J. A., Wilner, D. J., & Heyer, M. H. 1998, ApJ, 504, 223

Harten, A. 1984, SIAM Journal, 21 (1), 1

Hasegawa, T. I., & Herbst, E. 1993a, MNRAS, 261, 83

Hasegawa, T. I., & Herbst, E. 1993b, MNRAS, 263, 589

Herbst, E. 1993, in Dust and Chemistry in Astronomy, eds. Millar, T. J., & Williams, D. A. (Institute of Physics Publishing), p. 183

Hidaka, H., Watanabe, N., Shiraki, A., Nagaoka, A., & Kouchi, A. 2004, submitted to A&A

Hirota, T., Ito, T., & Yamamoto, S. 2002, ApJ, 565, 359

Hirota, T., Yamamoto, S., Mikami, H., & Ohishi, M. 1998, ApJ, 503, 717

Katz, N., Furman, I., Biham, O., Pirronello, V., & Vidali, G. 1999, ApJ, 522, 305

Lee, J-.E., Evans, N. J. II., Shirley, Y. L., & Tatematsu, K. 2003, ApJ, 583, 789

Lee, C. W., Myers, P. C., & Tafalla, M. 2001, ApJS, 136, 703

Léger, A., Jura, M., & Omont, A. 1985, A&A, 144, 147

Le Teuff, Y. H., Millar, T. J., & Markwick, A. J. 2000, A&AS, 146, 157

Li, Z.-Y., Shematovich, V. I., Wiebe, D. S., & Shustov, B. M. 2002, ApJ, 569, 792

Lis, D. C., Roueff, E., Gerin, M., Phillips, T. G., Coudert, L. H., van der Tak, F. F. S., & Schilke, P. 2002, ApJ, 571, L55

Mac Low, M.-M., & Klessen, R. S. 2004, RvMP, 76, 125

Millar, T. J., Bennett, A., & Herbst, E. 1989, ApJ, 340, 906

Myers, P. C., & Goodman, A. A. 1988, ApJ, 329, 392

Ogino, S., Tomisaka, K., Nakamura, F. 1999, PASJ, 51, 637

Ohashi, N., Lee, S. W., Wilner, D. J., & Hayashi, M. 1999, ApJ, 518, L41

Parise, B., Ceccarelli, C., Tielens, A. G. G. M., Herbst, E., Lefloch, B., Caux, E., Castets, A., Mukhopadhyay, I., Pagani, L., & Loinard, L. 2002, A&A, 393, L49

Parise, B., Catets, A., Herbst, E., Caux, E., Ceccarelli, C., Mukhopadhyay, I., Tielens, A. G. G. M. 2004, A&A, 416, 159

Pontoppidan, K. M., Dartois, E., van Dishoeck, E. F., Thi, W. -F., & d'Hendecourt, L. 2003, A&A, 404, L17

Prasad, S. S., & Huntress, W. T. Jr. 1980, ApJ, 239, 151

Pratap, P., Dickens, J. E., Snell, R. L., Miralles, M. P., Bergin, E. A., Irvine, W. M., & Schloerb, F. P. 1997, ApJ, 486, 862

Roberts, H., Herbst, E., & Millar, T. J. 2003, ApJ, 591, L41

Roberts, H., Herbst, E., & Millar, T. J. 2004, A&A, in press

Roser, J. E., Vidali, G., Manicò, G., & Pironello, V. 2001, ApJ, 555, L61

Ruffle, D. P., & Herbst, E. 2000, MNRAS, 319, 837

Ruffle, D. P., & Herbst, E. 2001, MNRAS, 324, 1054

Shematovich, V. I., Wiebe, D. S., Shustov, B. M., & Li, Z. Y. 2003, ApJ, 588, 894

Stantcheva, T., Caselli, P., & Herbst, E. 2001, A&A, 375, 673

Stantcheva T. & Herbst, E. 2004, A&A, 423, 241

Stone, J. M., Ostriker, E. C., & Gammie, C. F. 1998, ApJ, 508, L99

Suzuki, H., Yamamoto. S., Ohishi, M., Kaifu, N., Ishikawa, S., Hirahara, Y., & Takano, S. 1992, ApJ, 392, 551

Tafalla, M., Mardones, D., Myers, P. C., Caselli, P., Bachiller, R., & Benson, P. J. 1998, ApJ, 504, 900

Tafalla, M., Myers, P. C., Caselli, P., Walmsley, C. M., & Comito, C. 2002, ApJ, 569, 815

Tafalla, M., Myers, P. C., Caselli, P., & Walmsley, C. M. 2004, A&A, 416, 191

Tafalla, M., & Santiago, J. 2004, A&A. 414. 53

Tatematsu, K., Umemoto, T., Kandori, R., & Sekimoto, Y. 2004, ApJ, 606, 333

Terzieva, R., & Herbst, E. 1998, ApJ, 501, 207

Tielens, A.G.G.M. & Allamandola, L.J. 1987, in Interstellar Processes, eds. Hollenbach, D.J. & Thronson, H.A. Jr. (D. Reidel Publishing Company, Dordrecht), p.397

van der Tak, F. F. S., Caselli, P., Walmsley, C. M., Ceccarelli, C., Bacmann, A., & Crapsi, A. 2004, in : The Dense Interstellar Medium in Galaxies, eds. Pfalzner, S., Kramer, C., Staubmeier, C., & Heithausen, A. (Springer), p. 549

van der Tak, F. F. S., Schilke, P., Müller, H. S. P., Lis, D. C., Phillips, T. G., Gerin, M., Roueff, E. 2002, A&A, 388, L53

van Dishoeck, E. F., Blake, G. A., Janse, D. J., Groesbeck, T. D. 1995, ApJ, 447, 760

van Leer, B. 1977, J. Comp. Phys., 23, 276

van Leer, B. 1979, J. Comp. Phys., 32, 101

Vastel, C., Phillips, T. G., & Yoshida, H. 2004, ApJ, 606, L127

Walmsley, C. M., Flower, D. R., & Pineau des Forêts, G. 2004, A&A, 418, 1035

Ward-Thompson, D., Scott, P. F., Hills, R. E., & André, P. 1994, MNRAS, 268, 276

Watanabe, N., Nagaoka, A., Shiraki, T., & Kouchi, A. 2004, ApJ, in press

Watson, W. D. 1976, in Atomic and Molecular Physics and the Interstellar Matter. eds. Balian, R., Encrenaz, P., & Lequeuz, J. (Elsevier, Amsterdam), p.177

Zucconi, A., Walmsley, C. M., & Galli, D. 2001, A&A, 376, 650